

# A Quantitative Model of Energy Release and Heating by Time-dependent, Localized Reconnection in a Flare with a Thermal Loop-top X-ray Source

D.W. Longcope,<sup>1,†</sup> A.C. Des Jardins,<sup>1</sup> T. Carranza-Fulmer,<sup>2,3</sup> J. Qiu,<sup>1</sup>

<sup>1</sup> *Department of Physics, Montana State University, Bozeman, Montana 59717*

<sup>2</sup> *Montana State University, Solar Physics REU program*

<sup>3</sup> *City University of New York, New York, NY*

<sup>†</sup> *e-mail: dana@solar.physics.montana.edu*

## ABSTRACT

We present a quantitative model of the magnetic energy stored and then released through magnetic reconnection for a flare on 26 Feb 2004. This flare, well observed by RHESSI and TRACE, shows evidence of non-thermal electrons only for a brief, early phase. Throughout the main period of energy release there is a super-hot ( $T \gtrsim 30$  MK) plasma emitting thermal bremsstrahlung atop the flare loops. Our model describes the heating and compression of such a source by localized, transient magnetic reconnection. It is a three-dimensional generalization of the Petschek model whereby Alfvén-speed retraction following reconnection drives supersonic inflows parallel to the field lines, which form shocks heating, compressing, and confining a loop-top plasma plug. The confining inflows provide longer life than a freely-expanding or conductively-cooling plasma of similar size and temperature. Superposition of successive transient episodes of localized reconnection across a current sheet produces an apparently persistent, localized source of high-temperature emission. The temperature of the source decreases smoothly on a time scale consistent with observations, far longer than the cooling time of a single plug. Built from a disordered collection of small plugs, the source need not have the coherent jet-like structure predicted by steady-state reconnection models. This new model predicts temperatures and emission measure consistent with the observations of 26 Feb 2004. Furthermore, the total energy released by the flare is found to be roughly consistent with that predicted by the model. Only a small fraction of the energy released appears in the super-hot source at any one time, but roughly a quarter of the flare energy is thermalized by the reconnection shocks over the course of the flare. All energy is presumed to ultimately appear in the lower-temperature  $T \lesssim 20$  MK, post-flare loops. The number, size and early appearance of these loops in TRACE's 171 Å band is consistent with the type of transient reconnection assumed in the model.

## 1. Introduction

Since the introduction of magnetic reconnection Giovanelli (1947); Sweet (1958); Parker (1957); Petschek (1964), many models have proposed it as an element of flare-related phenomena, such as chromospheric ribbons Carmichael (1964); Sturrock (1968); Hirayama (1974); Kopp and Pneuman (1976), associated coronal mass ejections Moore and Labonte (1980); Forbes and Priest (1995), above-the-loop X-ray sources Masuda *et al.* (1994); Tsuneta *et al.* (1997) and supra-arcade downflows McKenzie and Hudson (1999); McKenzie (2000); Sheeley, Warren, and (2004).

The term “magnetic reconnection” is commonly used to refer to either or both of two different effects: topological changes to magnetic field lines and conversion of magnetic energy into other forms. Only the first effect, topological change, requires a parallel electric field and thereby qualifies as “magnetic reconnection” in the strictest sense. It has been successfully quantified by several kinds of observation. The amount of flux being topologically changed can be computed by tracking the ribbons across photospheric field in a flare Forbes and Priest (1984); Poletto and Kopp (1986); Qiu *et al.* (2002), computing the flux ejected by CMEs Qiu *et al.* (2007); Longcope *et al.* (2007), or measuring the fluxes of retracting downflows McKenzie and Savage (2009). Energy conversion, on the other hand, can occur together with the topological change, as in the diffusion-dominated Sweet-Parker models Parker (1957); Sweet (1958) or as a subsequent response to it, as in the Petschek model. The latter case would be more properly termed “post-reconnection energy conversion”, but Petschek’s model is customarily referred to as one of reconnection.

Recent theoretical progress has revealed that in order to be genuinely fast, the reconnection electric field must be localized to a small portion of a current sheet Birn *et al.* (2001); Biskamp and Schwarz (2001); Kulsrud (2001). Since such a small region will contain negligible magnetic energy, energy conversion must occur *away* from the region of flux transfer, as a post-reconnection *response* to small-scale topological change. This requirement of physical separation between the non-ideal electric field and the energy conversion offers the hope that energy conversion can be modeled without direct knowledge of, or appeal to, the specific physics dictating flux transfer.

In Petschek’s prototypical model of fast magnetic reconnection, energy conversion occurs at slow magnetosonic shocks (SMSs) originating in the small flux-transfer region Petschek (1964); Sonnerup (1970); Vasyliunas (1975); Soward and Priest (1982). While these models invoked a resistive electric field to transfer the flux, it has since been established that any localized process will produce the same external response provided the plasma may be treated by fluid equations (and thereby support collisional shocks) on its largest scales Erkaev, Semenov, and Jamitsky (2000). The two-dimensional, steady-state model has also

been generalized to transient reconnection Biernat, Heyn, and Semenov (1987); Nitta *et al.* (2001), reconnection between skewed magnetic fields (Petschek and Thorne 1967; Soward 1982; Skender, Vršnak, and Martinis 2003, *i.e.* with a magnetic field component, or “guide field”, in the ignorable direction, sometimes called “two-and-a-half” dimensions) and finally to transient reconnection in three dimensions Longcope, Guidoni, and Linton (2009b). We find that all such models predict very similar energetics since they all model external fluid responses to an assumed flux transfer of negligible dimension.

Tsuneta (1996) presented a thorough application of Petschek’s reconnection model to observations of a solar flare. He demonstrated that the temperature structure observed above the long-duration event on 21 Feb 1992 was consistent with the SMSs of two-dimensional Petschek reconnection. He showed further that local energy fluxes were consistent with the model, but could not, for a number of reasons, turn this into a global accounting of net energy released. First of all, the flare took place on the eastern solar limb making a reliable model of the coronal magnetic field difficult. Indeed, invoking Petschek’s original two-dimensional model tacitly neglects any possible magnetic-field component along the line of sight. Secondly, the reconnecting current sheet was probably a dynamical after-effect of a CME whose energetic contribution could overwhelm that of the flare itself. Finally, the impulsive phases of most large flares appear to include non-thermal particles, which fluid-based reconnection models cannot easily incorporate, but which account for a significant energy Lin and Hudson (1971); Strong *et al.* (1984); Emslie *et al.* (2004) .

Except for the adverse geometry, the difficulties faced by Tsuneta (1996) are likely to be common to most large flares. Non-thermal particles pose an especially difficult challenge for global energetics. While much progress has been made understanding the mechanism for their acceleration (Miller *et al.* 1997; Aschwanden 2002, for reviews), most models pre-suppose a non-ideal electric field, fluid turbulence, or plasma waves. Large-scale fluid models of reconnection are consistent, to some extent, with each of these, but do not include coupling to non-thermal particles. Since these particles ultimately account for a significant part of the released energy their effect is almost certain to be non-negligible.

A small subset of large flares show little evidence for non-thermal particles, but instead exhibit hard X-ray (HXR) thermal bremsstrahlung from a super-hot plasma ( $T \gtrsim 30$  MK). Rare as they are, these flares offer a unique opportunity to comprehensively quantify the energy release in a flare using a fluid reconnection model. Furthermore, these flares are often of the so-called *compact* variety and thus lack CMEs which could otherwise muddy the energy estimate. Lacking an eruption, the pre-flare magnetic field can be assumed to be near equilibrium and its energy more easily estimated. Such an ideal flare occurred on 26 Feb 2004 and was well observed by both RHESSI and TRACE at high cadence with little

interruption. This flare has been found to be one of the rare (one in ten) X-class flares unassociated with any CME Wang and Zhang (2007). We present here a model of how magnetic reconnection produced the phenomena observed in this flare, including estimates of the entire energy release process.

Spectrally resolved HXR images show a compact source probably located atop the flaring loops. This source is assigned an electron density which is high but typical of flaring plasma, ( $n_e \gtrsim 10^{11} \text{ cm}^{-3}$ ). The high density is required by both the large observed X-ray flux and in order that electrons of such high energies to be collisionally thermalized. High-temperature loop-top sources such as this have been observed before Acton *et al.* (1992); Petrosian, Donaghy, and McTiernan (2002); Jiang *et al.* (2006), and have proven particularly challenging to explain. We believe that shocks from fast reconnection offer a promising avenue for modeling the source, since they would both compress and heat the plasma.

The source’s persistence time vastly exceeds the time that it would take for the localized structure to conductively cool or to freely expand. Some models have addressed the former difficulty by proposing that a turbulent reduction of the electron thermal conductivity permits the high-temperature plasma to cool more slowly Jiang *et al.* (2006). This does not explain, however, how its high pressures are confined to the top of the loop. A second approach is to assume the observed, persistent structure is actually a super-position of sequential transient events; this approach is common in models of flaring loops Hori *et al.* (1997); Reeves and Warren (2002); Warren, Winebarger, and Hamilton (2002); Warren (2006). The temperature of these features does, however, change smoothly and gradually, in a manner resembling a slow cooling. Proposing that it consists of multiple isolated elements then requires an explanation for their smooth collective behavior. This is presumably a signature of the evolving energy conversion process — possibly magnetic reconnection.

In this work we show that magnetic reconnection occurring sporadically in small patches across a pre-flare current sheet will produce a super-position of high-density, high-temperature sources consistent with the observations on 26 Feb 2004. Moreover, the values of the temperature and emission measure, as well as their gradual temporal evolution, is consistent with the model. The specific physics responsible for transferring flux within the reconnection patches does not enter into these predictions and cannot therefore be constrained by the observations. The mean rate of transfer, which is to say the number of new patches per unit time, does enter, but this is a global quantity that can be measured Forbes and Priest (1984); Poletto and Kopp (1986); Qiu *et al.* (2002). While this kind of disordered process is less obviously related to Petschek’s model than a long, steady outflow jet, we show that it is consistent with the observed size and temperature of the loop-top source.

This combination of observations and model are presented as follows. The next section

describes the observational data of the flare. Section 3 then presents a model of the pre-flare magnetic field, including the geometry of the three-dimensional current sheet on which magnetic reconnection subsequently occurs. We then present, in section 4, a general model of transient, localized magnetic reconnection within a current sheet. The Alfvén speed and angular discontinuity characterizing the pre-reconnection current sheet directly predict the temperature of the reconnection outflow. We show that this prediction is common across all models of fast reconnection: steady state or transient, two-and-a-half or three-dimensional. In section 5 we apply this model to the observations of 26 Feb 2004. We maintain that evidence in this particular flare favors a transient reconnection model. We predict an emission measure that can be directly compared to observation. We use different means to measure the mean flux-transfer rate and find that all agree and predict flaring emission measure comparable to the observation. Section 6 uses the reconnection to model the full flare, including an account of its energetics. Finally, section 7 discusses the possible applicability of the new model to a broader class of flares.

## 2. The Flare: 26 Feb 2004

### 2.1. Active region 10564 – emergence

The 26 Feb 2004 flare (SOL2004-02-26T02:03:00L161C076) occurred within the complicated, but basically bipolar, active region 10564. The simple bipolar active region had one umbra of each polarity until, on 24 Feb, new flux began to emerge into it. This new flux eventually developed its own umbrae and the new positive and old negative penumbrae merged (see Figure 1). After roughly 50 hours of steady emergence an X-class flare occurred within the region.

To distinguish between new and old flux we partition the line of sight MDI magnetogram as shown in Figure 2. The radial component,  $B_r$ , is derived from the line-of-sight measurement assuming the field to be perfectly radial.<sup>1</sup> Those pixels exceeding  $|B_r| \geq B_{\text{thr}} = 125$  G are grouped into unipolar regions according to the horizontal gradient in  $B_r$  Barnes, Longcope, and Leka (2005); Longcope, Barnes, and Beveridge (2009a). The regions labeled  $N01$  and  $P03$  constitute the old bipole and all other partitions are from emergence since the beginning of 24 Feb.

---

<sup>1</sup>To assess the accuracy of the radial-field assumption Figure 1 has a longitude axis and marks showing the time the old polarities cross central meridian. Any systematic error would lead to an artificial center-to-limb variation centered at the  $\times$ .

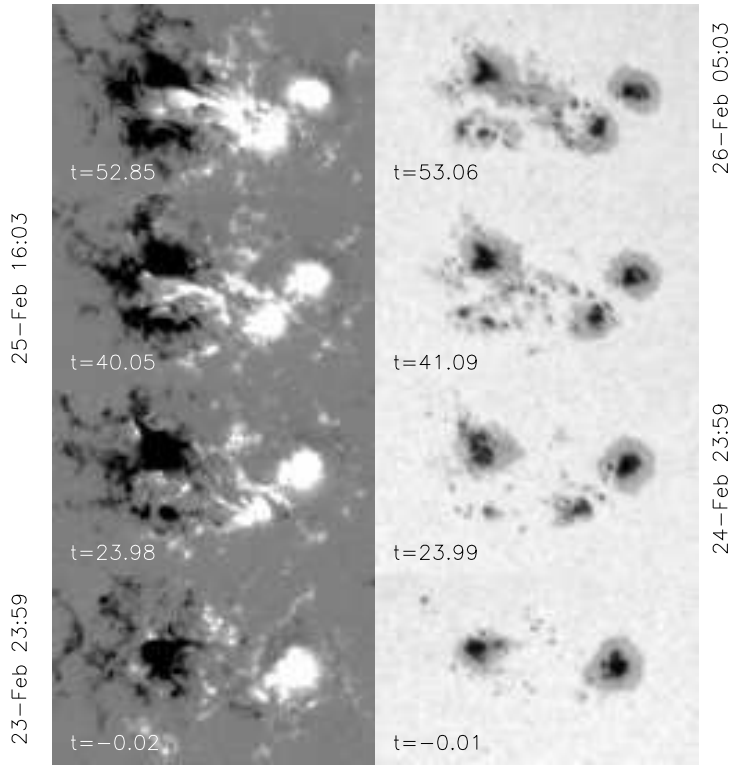


Fig. 1.— MDI data of new flux emergence in AR 10564. Rows are data from four successive times, progressing upward, spanning 54 hours. Printed on each panel is the time since 00:00UT on 26 Feb 2004. The left column is the line-of-sight magnetogram scaled between  $\pm 1000$  G; the right is the continuum image.

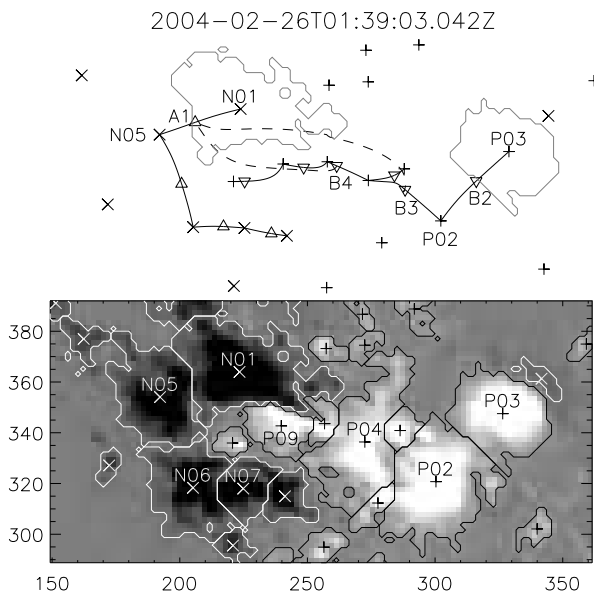


Fig. 2.— Partition of the line-of-sight magnetogram from just before the flare. The lower panel shows the magnetogram, scaled to  $\pm 1000$  G. Lines denote the boundaries of a partition, and + and  $\times$  are the centroids of each region. The upper panel shows the same centroids along with null points (triangles) and the principal spines (solid) connecting them. The dashed curves are separators connecting null point  $A1$  to  $B3$  and  $B4$ .

The net flux and centroid of each region ( $\Phi_i$  and  $\bar{x}_i$ ) is found by integrating its surface field. The time evolutions of old flux,  $\Phi_{P03}$  (positive) and  $\Phi_{N01}$  (negative), are shown as dashed curves in Figure 3. At the beginning of the data each has approximately  $8 \times 10^{21}$  Mx of flux. Over the course of our data set the fluxes in each polarity gradually decreases until they are  $\Phi_{P03} = 5.6 \times 10^{21}$  Mx and  $\Phi_{N01} = 7.4 \times 10^{21}$  Mx at the time of the flare. The new flux, comprising the remainder of the regions in the partition, increases much more rapidly over this period reaching twice that of the old flux ( $|\Phi| \simeq 13 \times 10^{21}$  Mx) by the time of the flare. The emergence is steady and there is no clear feature in the evolution at the time of the flare (vertical dashed line). There is a small excess of negative flux (broken line) due to the omission of positive flux either outside the field of view or below the threshold strength,  $B_{\text{thr}} = 125$  G.

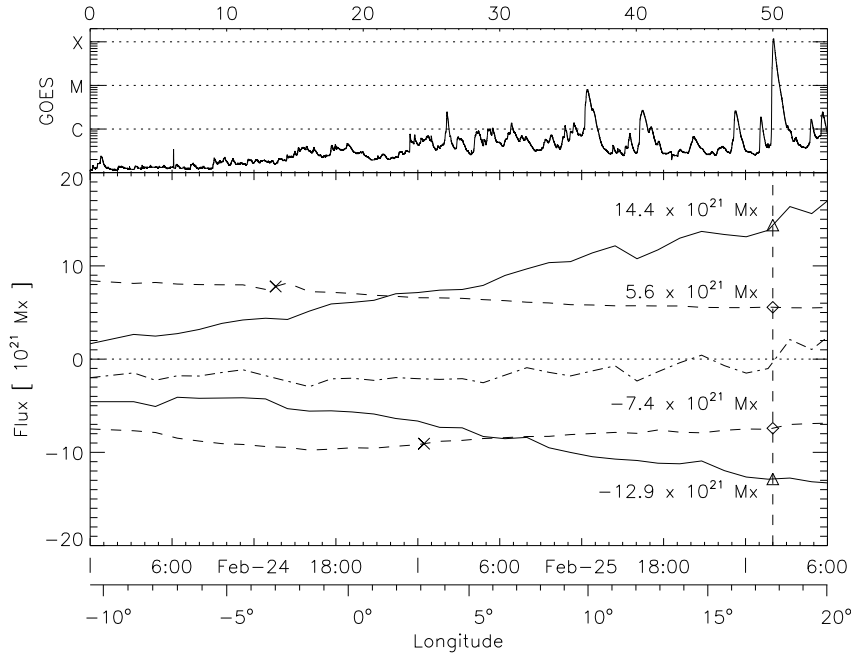


Fig. 3.— The fluxes in the new (solid) and old (dashed) polarities of AR 10564; the broken line is the total signed flux of all regions. The value at the time of the flare, 26 Feb 2:03UT (vertical dashed line), is given and indicated with a symbol. The signed sum of all fluxes, shown as a broken line, is close to zero. The times at which each of the old polarities crosses central meridian is shown with an  $\times$ , and the longitude of their mid-point is shown by the bottom axis. The top panel shows the GOES  $1\text{\AA} - 8\text{\AA}$  flux. The top axis gives hours past 24 Feb 00:00.

We interpret flare observations in terms of a magnetic model built using these photospheric observations combined with assumptions about flux emergence. The partitioning of

the photospheric field described above makes no assumption about the state of the coronal field, but does provide a framework for quantifying its connectivity Longcope and Klapper (2002). Regardless of the state of the coronal field, every coronal field line can be assigned to a domain based on the photospheric regions of its footpoints: its connectivity. Different coronal fields have different connectivity and the level of difference between two possible fields is quantified by the differences in domain fluxes Longcope, Barnes, and Beveridge (2009a). We use the potential field extrapolated from the pre-flare magnetogram of 1:39 (Figure 2) as a reference for constructing such differences. The potential field has the minimum possible magnetic energy so the degree by which a given field differs from it relates to the amount for free energy in the field Longcope (2001); Longcope and Magara (2004).

Provided the post-flare coronal field has lower magnetic energy than the pre-flare field, we expect its connectivity to be closer to that of the potential field. The potential field connectivity is characterized in terms of the magnetic skeleton Priest, Bungey, and Titov (1997); Longcope and Klapper (2002); Beveridge and Longcope (2005), illustrated by the top panel of Figure 2. This stylized figure shows sources (+s and ×s) and several of the magnetic null points (triangles) of the potential field. Solid curves show the spine lines from each null point, and dashed lines are two separators which extend into the corona from null points *A1*, *B3* and *B4*. The spine lines trace out the edges of separatrix surfaces which divide the coronal magnetic field into different domains. Most significant for the present case, they divide the pre-existing coronal field, anchored to *P03* and *N01*, from newly emerging field.

The pre-flare field will differ significantly from the potential field since it must contain significant currents. Rather than try to measure these currents we infer them from the connectivity after assuming that no significant reconnection occurred prior to the flare. This means that in the pre-flare field the old photospheric regions, *P03* and *N01*, remain unconnected to the others, such as *P09* or *N07*, which recently emerged. The potential field, and therefore the post-flare field, contains significant connections between new and old regions *P09* and *N01*, due to their proximity. By our flux-emergence assumption, however, this connection contains zero flux in the pre-flare field. It is differences such as this that lead to large free energies in the pre-flare field. The forging of new connections through reconnection will reduce this difference thereby releasing stored magnetic energy and presumably powering the flare.

## 2.2. The flare loops

EUV images provide evidence supporting our assumption that flare-related reconnection creates field lines with new connectivity. TRACE obtained 171Å images at a 30-second

cadence throughout the flare. Figure 4 shows an image from before the flare (1:31) and seven subsequent images during the flare. Post-flare loops occupy the region between by the spine curves, corresponding to a coronal volume beneath the associated separatrices. In images from early in the flare the  $171\text{\AA}$  emission is primarily chromospheric, including moss, foot-points and flare ribbons (e.g. 1:55:14). Following a common pattern Gorbachev and Somov (1988); Longcope *et al.* (2007), the flare ribbons follow the topological spines. Coronal loops are visible as early as 1:57 and become the primary features by 2:04:14.

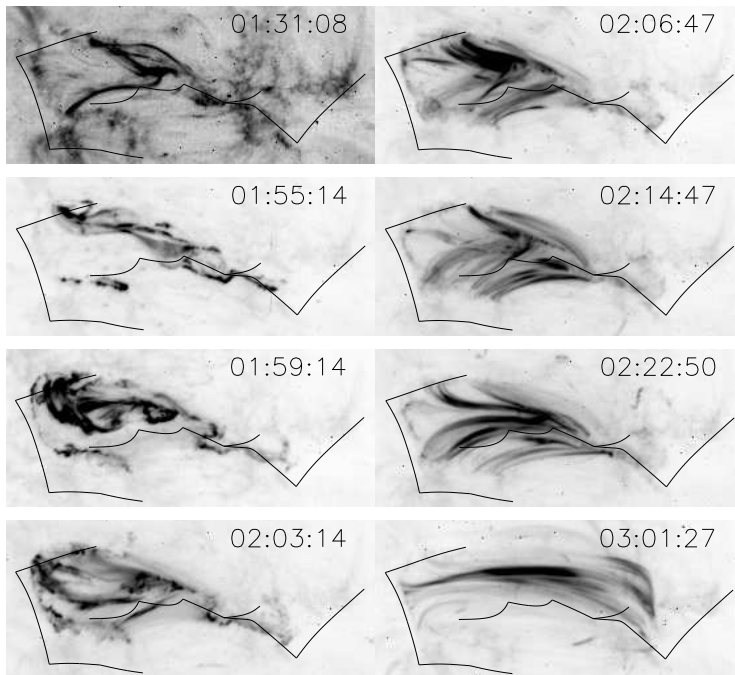


Fig. 4.— TRACE  $171\text{\AA}$  images from times before (1:31) and during the flare, shown in inverse greyscale. The grey scale is enhanced by a factor of eight in the first image and by  $4/3$  in the final three (2:14 – 3:01). Dark lines in each frame show the spines from the magnetic skeleton from Figure 2.

The visible coronal loops are summarized in Figure 5. 143 loops were visually identified and manually traced in the collected 30-second cadence  $171\text{\AA}$  TRACE images. Those loops persisting longer than the median lifetime, 6.0 minutes, are plotted over the partitioned magnetogram with color indicating the time of first appearance. Early, short loops connect new positive regions  $P09$  and  $P04$  to the old nearby region  $N01$ . Later in the flare, longer

connections are made between *N01* and the more distant region *P02*. This is still newer than region *P03* which was part of the original bipole. The apparent lengths of these loops increase with time approximately linearly according to the empirical relation

$$L_{\text{EUV}}(t) = \dot{L}(t - t_0) + L_0 \quad , \quad (1)$$

where  $\dot{L} = 4.7 \text{ Mm hour}^{-1}$  and  $L_0 = 6.3 \text{ Mm}$  using  $t_0 = 2:00:00$ . At the onset of the flare new loops were appearing at a rate of four per minute, as indicated by the dotted line in the bottom panel.

The overall time history of the flare is summarized in the composite light curve of Figure 6. The first evidence of the flare is an impulsive brightening, at 1:53:50, in high energy X-rays (RHESSI 25 – 50 keV channel at top). The lower energy X-ray channels begin rising at about this same time, as do both of the GOES X-ray channels. The first 171Å image after a five-minute gap (1:55:14) has total emission clearly elevated from the pre-flare level. Three minutes after the initial burst, at 1:56:40, all X-ray channels rise more rapidly to a higher level. It is during the times following this second rise that TRACE 171Å images are dominated by loops.

### 2.3. Super-hot thermal loop-top source.

Hard X-ray emission from the flare occurs in two phases with distinct spectral forms typified by the examples shown in Figure 7. Each spectrum is a 20-second integration of RHESSI detector 3. Plasma properties such as temperature and emission measure are found by fitting the spectra with the OSPEX software package Schwartz (1996). In determining the best-fit model for each spectrum examined here, the following considerations were taken into account: spectral analysis from a single detector at a time, individual background subtraction for each energy range (6 – 12, 12 – 25, 25 – 50, 50 – 100 keV), albedo correction, the presence of instrumental lines at 8.5 and 10.5 keV (not shown in the figure), modifications necessary due to individual detector response differences and pulse pile-up and the attenuator change from A1 (thin only) to A3 (thick and thin) at  $\approx 1:57$  and back to A1 at  $\approx 2:07$ .

For every 20 sec. time interval from 01:54 – 02:10, we modeled spectra in two distinct ways. First we fit a thermal bremsstrahlung plus a non-thermal thick target (power law). Next we did a separate fit to two thermal bremsstrahlung components (a two-temperature fit). We found that the first phase of the flare (approximately 01:53:50 – 01:56:40) is best characterized by the first fit, a thermal plus non-thermal spectral model; we refer to this phase of the flare as the non-thermal phase. The second phase (approximately 01:56:40 – 02:10) is best fit by the two temperature model with no non-thermal contribution; we refer

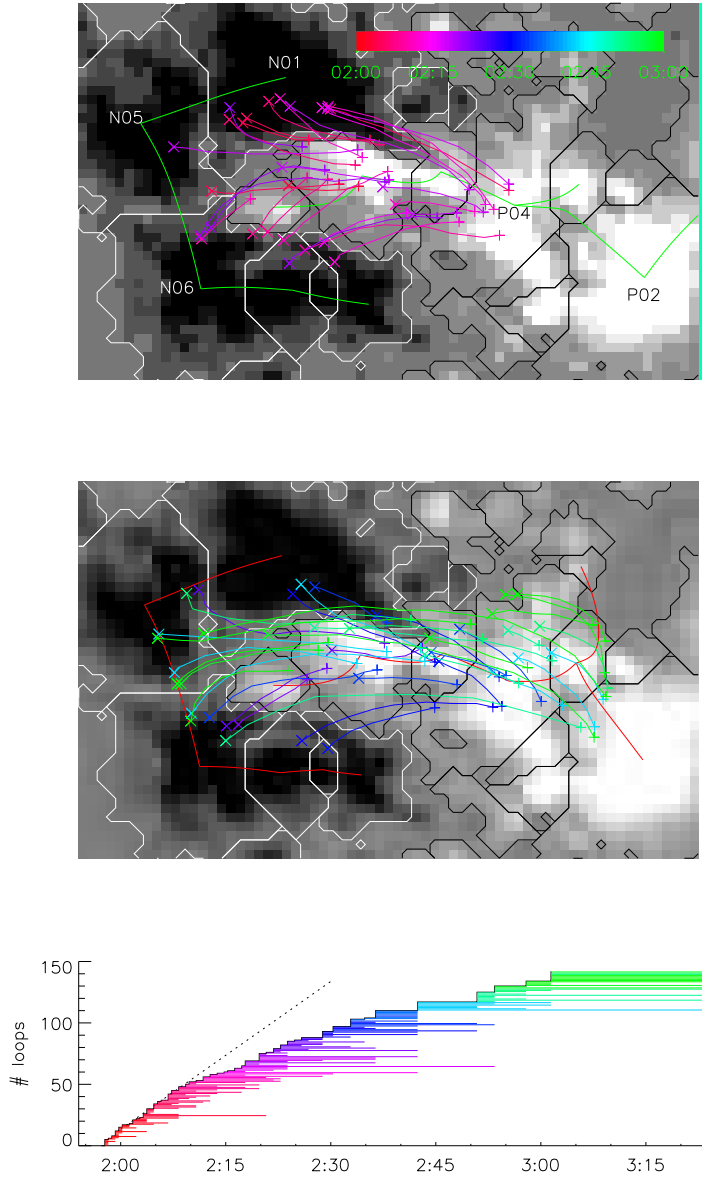


Fig. 5.— Coronal loops visible in TRACE 171Å images are shown as color curves atop the partitioned MDI magnetogram. Colors from red to green represent times from 2:00 to 3:00UT, as indicated in the top color bar. The upper panel shows the loops which appear before 2:18, and the middle panel shows later loops. For clarity, only those loops visible for longer than the median lifetime are shown. The bottom panel shows the accumulated number of loops visible before any time. Horizontal bars show the lifetime of each loop, colored with the same code as the loops themselves.

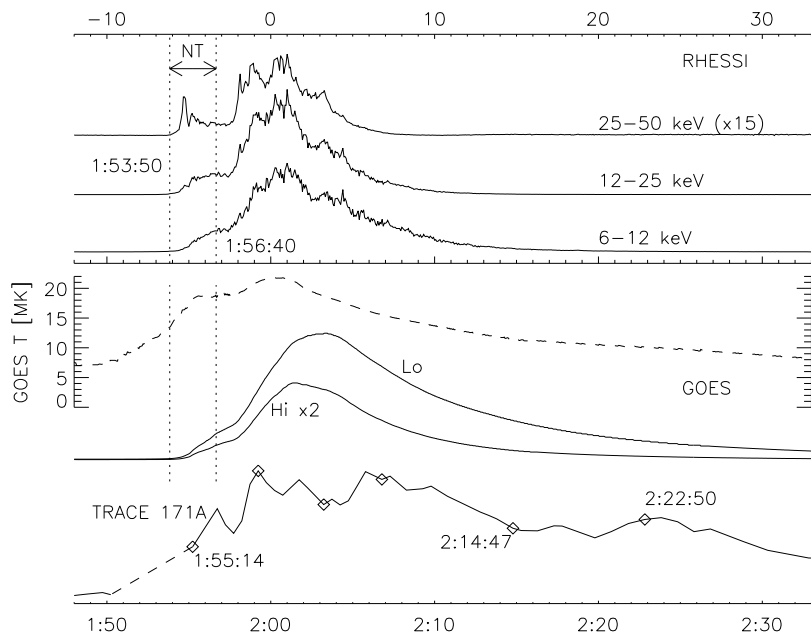


Fig. 6.— A composite light curve of the flare on 26 Feb 2004. All curves show intensity on a linear scale. The bottom curve is the integrated intensity of TRACE 171Å from the region shown in Figure 4. The zero level is suppressed, but the level prior to 1:50 shows the pre-flare background. The dashed section is a 5-minute data gap and diamonds show the times at which the central six panels of Figure 4. Above this are the curves from the low energy (Lo, 1 – 8Å) and high energy (Hi, 0.5 – 4Å) channels of GOES; the latter has been multiplied by two to facilitate comparison. The dashed curve above them is the plasma temperature derived from the ratio of GOES energy channels Garcia (1994). Top curves are integrated intensity from RHESSI channels, from bottom to top, 6 – 12, 12 – 25 and 12 – 25 keV. Vertical dotted lines show the beginning and end of the non-thermal phase of the flare.

to this phase as the thermal phase. During the thermal phase, the higher energy end of the spectrum ( $T \gtrsim 12$  keV) is consistently better fit by a super-hot thermal bremsstrahlung component than by a thick target power law component. In the 01:58:10 spectrum in Figure 7, the super hot component (magneta) has a temperature of 46 MK

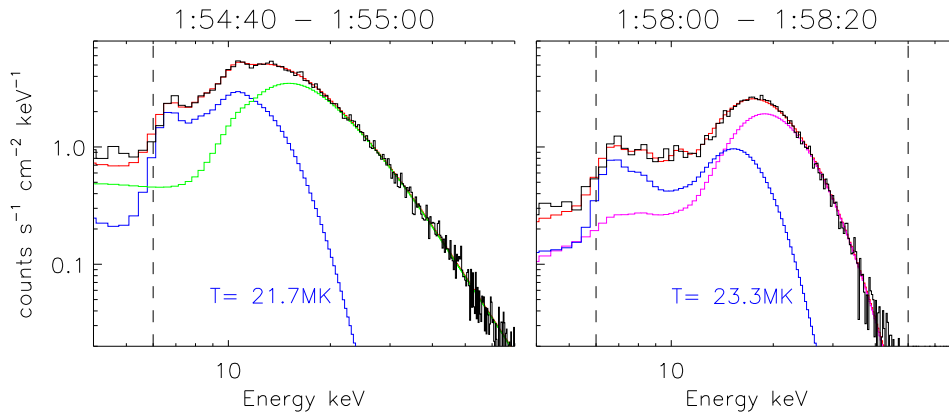


Fig. 7.— RHESSI spectra from detector 3 integrated over 20 seconds plotted in black and multi-component fits. Separate components of each fit are plotted in different colors, and their sum is the red curve. The fit was performed over the region delineated by the vertical dashed lines. (left) An early phase in the flare, centered at 1:54:50, fit by one thermal component ( $T = 22$  MK, blue) and thick-target emission from a non-thermal component with power-law spectral index  $\delta = 6.4$  (green). (right) A later phase in the flare centered at 1:58:10 fit by two thermal components:  $T = 46$  MK (magneta) and  $T = 23$  MK (blue).

The spatial morphology of X-ray emission also differs between the two phases, as illustrated by the RHESSI CLEAN images shown in Figure 8. During the non-thermal phase (Figure 8a) the highest energy emission (25 – 50 keV, green) originates in two distinct sources located on opposite sides of the PIL. These are presumably from non-thermal particles striking the chromospheric footpoints of the reconnected field lines, perhaps linking  $P09 - N06$ . While the lower energy emission (6 – 25 keV, red and blue) extends over the footpoints, it is more concentrated between the two sources. This point is presumably closer to the apex of the loop, or the site of the reconnection. It is notable that the peak of the 6 – 12 keV emission (red) occurs near the separator field line (magenta).

During the thermal phase (Figures 8b – d) the high and low energy emission originate from a single source near the separator field line. It is elongated approximately parallel to the separator, with length  $\approx 16$  Mm and width  $\approx 9$  Mm. Based on the magnetic geometry we believe this source is at the top of the post-flare loop system; it is a loop-top source viewed from above. By 2:05 (Figure 8d) the count rate in the highest energy channel (25 –

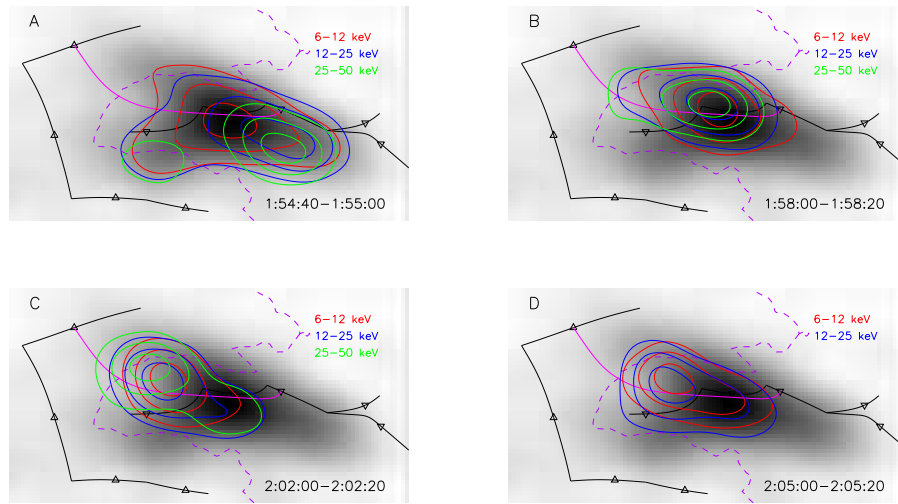


Fig. 8.— RHESSI images formed using the CLEAN algorithm on 20-sec integrations of multiple detectors. The grey scale in all images is from low-energy channel (6 – 12 keV) integrated beginning at 1:54:00. Contours are at levels of 50%, 70% and 90% of maximum for energy levels 6 – 12 keV (red), 12 – 25 keV (blue) and 25 – 50 keV (green). The panels show integrations beginning at A: 1:54:40, B: 1:58:00, C: 2:02:00 and D: 2:05:00. Also shown are the spines (black), null points (triangles), one separator (magenta) and polarity inversion line (violet dashed).

50 keV) had fallen too low to permit accurate imaging.

Spectra were formed from both detectors 3 and 4 over each 20-second interval after 1:54:40. All spectra resemble one of the typical cases shown in Figure 7, but with different fitting parameters. Time histories of the best-fit temperatures and emission measures of each component are shown in Figure 9. Spectra at times before 1:56:40 have non-thermal (NT) components and are best fit by a thick target power law and one thermal component whose temperature and emission measure are plotted alone. All later spectra are fit by two temperatures. By 2:07:00 the two temperatures are sufficiently close that it becomes difficult to discriminate between the components. As a result, the fits from the different detectors give notably different values as indicated by larger error bars. As early as 2:05:00, the time of image 8d, the temperature of super-hot component had fallen sufficiently low (26 MK) that it does not contribute enough signal to the 25 – 50 keV channel to permit accurate imaging; for this reason there is no green contour in that image.

The super-hot component reaches as high as  $T = 48$  MK at the beginning. It decreases on an approximately exponential decay (dashed curve) with a time constant of 14.2 minutes, while the cool component decays even more slowly. It is notable that the cool component matches the properties derived from the two GOES channels (after subtracting a background level determined from an interval prior to 1:00); the GOES-derived emission measure appears to be larger than the RHESSI value by roughly a factor of 2 Hannah *et al.* (2008).

### 3. Model of the pre-flare magnetic field

The picture which emerges from the foregoing data is of a sudden burst of reconnection between the old bipole and the newly emerged flux. In the seminal model of such reconnection, proposed by Heyvaerts *et al.* (1977), a current sheet forms between the two flux systems. Reconnection across this sheet releases the energy which powers the flare. A potential field above that configuration would contain a single coronal null point from which four separatrices divide the coronal flux into four domains: new flux, old flux and two mixed old/new domains. Remaining potential during emergence requires reconnection across the null point in order to convert new and old flux into the mixed type field lines. Without reconnection a current sheet forms at the erstwhile null point.

The Heyvaerts *et al.* (1977) model is two-dimensional and the emerging field is purely anti-parallel to the overlying field. In the present case, however, the emerging flux is largely parallel to the existing bipole  $P03 - N01$ . This leads to a modified three-dimensional model in which the potential field contains a separator rather than a coronal null point. A potential

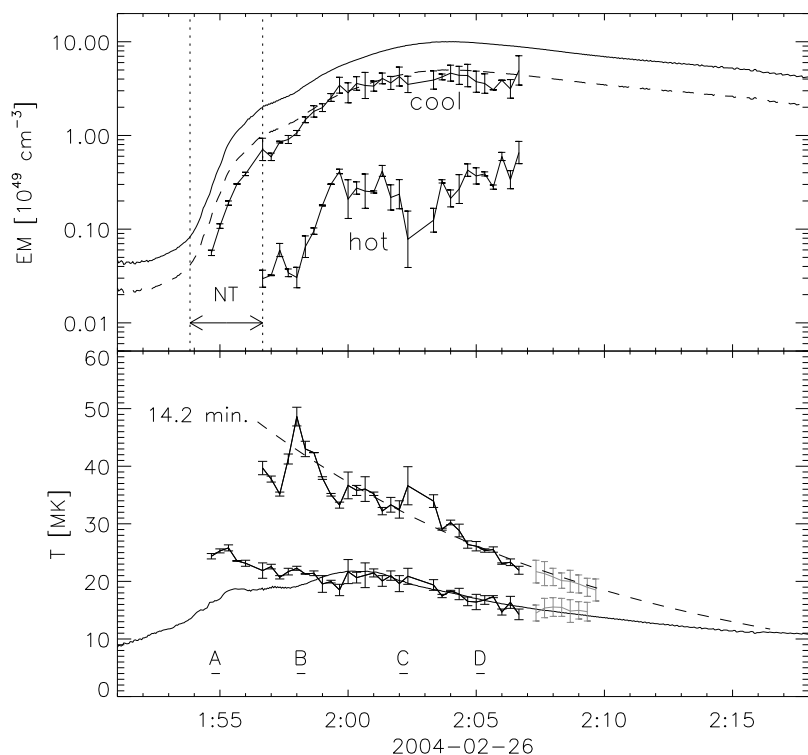


Fig. 9.— The temperatures and emission measures of the two thermal components from detectors 3 and 4. Curves show the simple average of temperatures from the two detectors (bottom) and geometric means of emission measures (top). Error bars show the values from each detector. The smoother solid curves are the values derived from the two GOES channels. The dashed curve is the GOES-derived emission measure divided by a factor of 2, after Hannah *et al.* (2008). Lighter points show times after 2:07, where the two components were more difficult to discriminate. The dashed temperature curve is an exponential fit to the super-hot component; its decay time is 14.2 minutes. The imaging intervals, A – D, from Figure 8 are indicated along the bottom.

field extrapolated from the magnetogram of Figure 2 contains no coronal nulls but many separators; two separators are shown in the upper panel. Each separator is a magnetic field line ( $\mathbf{B} \neq 0$ ) lying at the intersection of two separatrices. Together these separatrices separate four different field line connectivities and the separator lies between all four.

In analogy to the two-dimensional model of Heyvaerts *et al.* (1977), emergence without reconnection leads to a current ribbon approximately following the path of the potential-field separator. Figure 10 shows the configuration of such a current ribbon along the separator connecting photospheric null points  $A1$  and  $B4$ . There is a component of magnetic field parallel to the current, often called a *guide field*. In spite of its three-dimensional structure the equilibrium structure of this current ribbon can be approximated using the two-dimensional model of Green (1965) and Syrovatskii (1971).

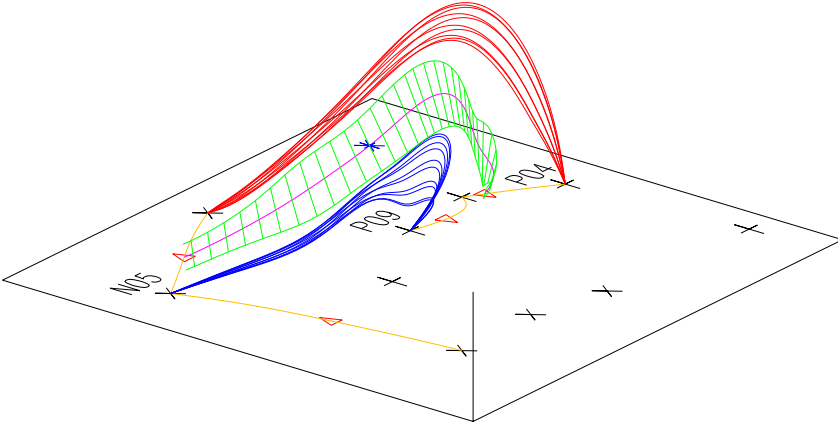


Fig. 10.— A perspective view of a current ribbon along the separator field line connecting null points  $B4$  and  $A1$  (magenta). The current sheet is indicated by green ribs and the current flows roughly parallel to the magenta separator. Examples of post reconnection field lines are indicated by red ( $P04 - N01$ ) and blue ( $P09 - N05$ ). A blue asterisk shows a point along the separator located  $z = 7.9$  Mm above the photosphere.

To analyze the current ribbon, consider a plane perpendicular to the separator field line at one single point, such as the blue asterisk in Figure 10. Take this as the origin of the plane with local coordinates  $y$  and  $z$ . In the neighborhood of the origin the potential magnetic field within this plane is

$$\mathbf{B}^{(v)}(y, z) = B_g \hat{\mathbf{x}} - B'_\perp (y \hat{\mathbf{z}} + z \hat{\mathbf{y}}) , \quad (2)$$

where  $B'_\perp$  is the local field gradient at the origin Longcope and Silva (1998); Longcope and Magara (2004). At the coronal point indicated in Figure 10,  $B_g = 331$  G and  $B'_\perp = 34$  G Mm $^{-1}$ .

The plane’s coordinates have been oriented so the field is radial along diagonals  $45^\circ$  from the coordinate axes. Unlike the two-dimensional case, these diagonal lines cannot be associated with the field’s separatrices, since those are global features not derivable from local properties of the field.

The perpendicular extent of the current sheet follows the two-dimensional model of Greene (1965) and Syrovatskii (1971). The net current in the sheet,  $I$ , determines its width

$$\Delta = 4\sqrt{\frac{|I|/c}{B'_\perp}}, \quad (3)$$

where  $B'_\perp > 0$  but  $I$  may be of either sign. The sheet extends along the  $\pm\hat{y}$  direction when  $I > 0$  and along  $\pm\hat{z}$  when  $I < 0$ , as shown in Figure 11. Since  $B'_\perp$  varies along the separator so does the width of the current ribbon, as evident in Figure 10. It does, however, carry the same current  $I$  over its entire length,  $L$ .

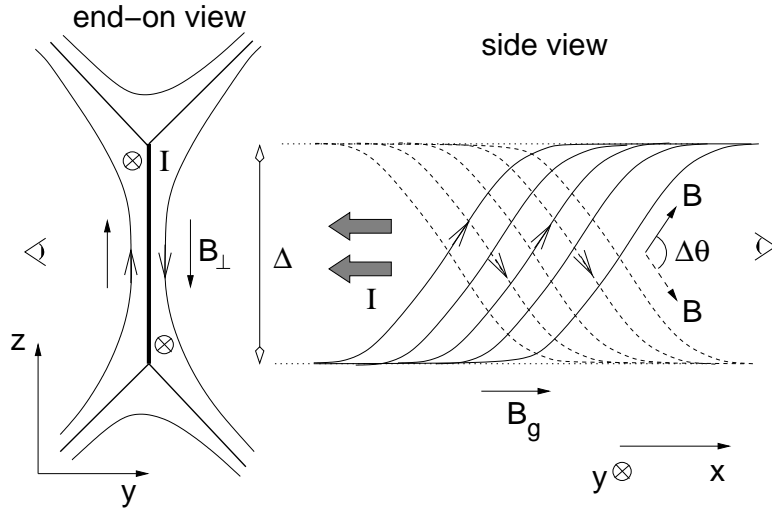


Fig. 11.— The geometry of a current sheet with a guide field component. The left panel shows the conventional “end-on view” of the sheet, along its current  $-\hat{x}$ . Two Y-type neutral points, separated by  $\Delta$  define the ends of the sheet. Viewing this from the left provides the less-conventional “side view”, shown in the right panel. The Y-type neutral lines extend horizontally along the top and bottom of the sheet (dotted lines). The guide field is directed to the right ( $+\hat{x}$ ) on both sides of the sheet. The field on the near side (solid) is directed upward while that on the far side (dashed) is directed downward. The angle between these field lines is  $\Delta\theta$ .

The current sheet arises from a hypothesized absence, during pre-flare build-up, of reconnection required to achieve a potential field state. A potential field extrapolated from

the magnetogram of Figure 2, contains field lines linking, for example, the new pole  $P04$  to the old pole  $N01$ . In fact roughly 60% of the flux from  $P04$  connects to  $N01$  for a total flux  $\Psi_{4-1}^{(v)} = 2.8 \times 10^{21}$  Mx, where the superscript is a reminder that this value pertains to the potential (vacuum) field.

All new polarities presumably emerged connected only among one another. In this case a connection between new and old regions would contain zero flux,  $\Psi_{4-1} = 0$ , in contrast to the non-zero flux in the potential field. It is this discrepancy

$$\Delta\Psi_{4-1} = \Psi_{4-1} - \Psi_{4-1}^{(v)} \quad , \quad (4)$$

between the potential field connectivity and the actual connectivity which leads to the separator current Longcope (2001). For small values, the net current follows a simple self-inductance relation

$$\frac{I}{c} \sim \pm \frac{\Delta\Psi}{4\pi L} \quad , \quad (5)$$

where we have omitted, for clarity, a factor depending on  $\ln(|I|)$ .

The sense of current depends on the sense of change,  $\Delta\Psi$ , relative to the sense of the potential field. Potential field links the separator of Figure 10 in a positive sense: right-handed following the separator in the direction of the guide field. Before any reconnection,  $\Psi_{4-1} = 0$ , so the self flux from the current ribbon must be directed through the separator in the opposite sense. Thus the current must flow anti-parallel to the guide field:  $I < 0$ . This produces the roughly vertical sheet shown in Figure 10.

The separator shown in Figure 10 has length  $L = 54$  Mm and will therefore, according to eq. (5), carry  $I/c \simeq 4 \times 10^{10}$  G cm (*i.e.* 400 GAmperes) prior to any reconnection. This is confined to a current sheet whose width at the coronal point ( $B'_\perp = 34$  G Mm $^{-1}$ ) is  $\Delta \simeq 14$  Mm. It is natural that the half-width of this vertical sheet is close to the height of the point since the current sheet must totally separate the new and old fluxes. Had the absence of reconnection across this one separator been the only constraint on the coronal field, the field would contain free energy

$$\Delta W \simeq \frac{I}{2c} \Delta\Psi = \frac{\Delta\Psi^2}{8\pi L} \quad , \quad (6)$$

which is  $\Delta W = 5 \times 10^{31}$  ergs. Although there are numerous other separators imposing other constraints, this crude estimate is consistent with the amount of energy ultimately released in the flare.

While the width of the sheet,  $\Delta$ , depends on global properties of the field, its thickness,  $\delta$ , depends on non-ideal processes significant inside the sheet. For a Sweet-Parker solution in the presence of uniform resistivity,  $\eta$ , the thickness would be  $\delta \simeq \Delta S_\Delta^{-1/2}$  where the current

sheet Lundquist number is

$$S_{\Delta} = \frac{\Delta v_{A,\perp}}{\eta} = \frac{|I|}{I_{\text{sp}}} , \quad \frac{I_{\text{sp}}}{c} = \eta \sqrt{\frac{\rho}{4\pi}} . \quad (7)$$

Spitzer resistivity in a coronal plasma ( $T = 10^6$  K and  $n_e = 10^{10} \text{ cm}^{-3}$ ) yields a characteristic current  $I_{\text{sp}} \simeq 10^{-2}$  Amps, for which the Lundquist number will exceed  $10^{12}$ . In this case the equilibrium width of the current sheet would be  $\delta \simeq 14$  m. Sweet-Parker reconnection at such a high Lundquist number transfers flux very slowly, making it essentially “non-reconnection”. In spite of the large current density the energy dissipation,  $P \approx (I/c)d\Psi/dt \approx \Delta W/\tau_{sp}$ , is negligibly small. Thus we would expect signatures of a pre-flare current sheet to be extremely weak, if observable at all. This is constant with the absence of any current-sheet signature from pre-flare EUV images.

Given this slow reconnection it is possible for the current sheet to exist for any portion of the 50-hour build-up phase. The flare itself must arise from a rapid transfer of flux across the current sheet. In other words, the current sheet is necessary but not sufficient for reconnection.

In light of the coincidental appearance of numerous thin coronal loops of the new connectivity it seems that flux transfer was unsteady and spatially intermittent rather than a steady, extended electric field along the separator current sheet. Indeed, it has become recognized that localized electric fields are a necessary condition for fast magnetic reconnection Biskamp and Schwarz (2001); Kulsrud (2001).

#### 4. A Model of Time-Dependent Localized Reconnection

The localized reconnection will occur across a current sheet where field lines of different connectivity come into close enough proximity to be interconnected by localized processes. As a model of the process consider a Green-Syrovatkii current sheet with a guide field  $B_g$  such as that from Figure 11. Such a current sheet separates field lines of the same magnitude but differing in angle by  $\Delta\theta = 2 \tan^{-1}(B_{\perp}/B_g)$ . The strength of the reconnecting component depends on the width of the current sheet,  $B_{\perp} = B'_{\perp} \Delta/2$ , so the reconnection angle is

$$\Delta\theta = 2 \tan^{-1} \left( \frac{\Delta}{2B_g/B'_{\perp}} \right) . \quad (8)$$

The separator in our pre-flare field is characterized by a dimension  $B_g/B'_{\perp} \simeq 10$  Mm. When the current sheet width reaches  $\Delta = 14$  Mm the reconnecting field angle is  $\Delta\theta = 70^\circ$ .

The computation above reveals that current sheet reconnection occurs in the presence of a significant guide field. A transient and spatially localized reconnection event in such a current sheet will produce a flux tube as illustrated in Figure 12. While all field lines adjacent to the current sheet were initially in equilibrium, the reconnection produces sudden disequilibrium from very sharp bends in the new tubes. These bends produce a rapid retraction of the tube; each tube pulls itself straight by sliding through the sheet Linton and Longcope (2006); Linton, Devore, and Longcope (2009); Longcope, Guidoni, and Linton (2009b). The retraction is governed by dynamics independent of the process which created the non-equilibrium tubes.

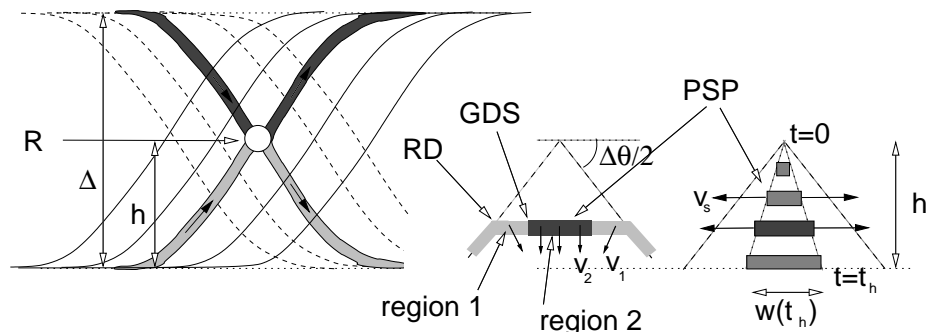


Fig. 12.— Patchy, transient reconnection in a current sheet. Reconnection within patch  $R$  creates two flux tubes (light and dark grey) shown in the left panel. Each of these retracts through the sheet; the central panel illustrates the retraction of the lower tube. Rotational discontinuities (RDs) propagate along the tube at the Alfvén speed. Central compression creates two gas dynamic shocks (GDSs) confining a hot, dense plug of post-shock plasma (PSP). This moves downward with the flux tube at speed  $v_z$  and expands horizontally at the shock speed  $v_s$ . The right panel shows the plug at successive times culminating in  $t = t_h$ , when it reaches the Y-type neutral line along the bottom of the sheet.

#### 4.1. Structure of reconnection outflow

Post-reconnection retraction releases magnetic energy by shortening the tube on the Alfvén time characteristic of magnetically-driven dynamics. The initial bend decomposes into two rotational discontinuities (RDs) propagating at the Alfvén-speed and two slow mode shocks (SMSs) or gas-dynamic shocks (GDSs). The RDs produce the rapid shortening, but they do so without changing temperature or density of the plasma. This rapid shortening takes the form of Alfvén speed motions  $\mathbf{v}_1$  directed partly inward in order to decrease the length. This parallel compression is therefore much faster than the slow magnetosonic waves which govern its dynamics, and the flows collide in SMSs or GDSs.

Longcope *et al.* (2009b; hereafter called LGL09) presented a three-dimensional model of such transient, patchy magnetic reconnection. They used thin-flux tube dynamics to describe the retraction and compression. They found dynamical evolution following the diagram in the center panel of Figure 12, with purely hydrodynamic GDSs formed by the converging flows.

In the model of LGL09 each RD in the downward-moving tube produces a flow, designated region 1, directed along the bisector of the bend,

$$\mathbf{v}_1 = \mp 2v_{A,0} \sin^2(\Delta\theta/4) \hat{\mathbf{x}} - v_{A,0} \sin(\Delta\theta/2) \hat{\mathbf{z}} \quad (9)$$

where  $v_{A,0}$  is the Alfvén speed in the background magnetic field outside the current sheet. The two RDs direct flows inward in opposing horizontal senses. In a reference frame moving downward with the horizontal segment each inflow has gas-dynamic Mach number (LGL09)

$$M_1 = \frac{|v_{x,1}|}{c_{s,1}} = \sqrt{\frac{8}{\gamma\beta_0}} \sin^2(\Delta\theta/4) \quad , \quad (10)$$

where  $c_{s,1}$  is the sound speed in the pre-reconnection (and pre-shock) plasma. Except in cases of very small reconnection angles  $\Delta\theta$ , the small value of pre-reconnection  $\beta$ , denoted  $\beta_0$ , ensures very large inflow Mach number.

The collision of these two inward flows brings the plasma to rest at two gas-dynamic shocks (GDSs). The density increase across these shocks follows from the gas-dynamic conservation laws (LGL09)

$$r = \frac{\rho_2}{\rho_1} = \frac{\sqrt{9 + 4M_1^2} + 2M_1}{\sqrt{9 + 4M_1^2} - M_1} \quad , \quad (11)$$

assuming the shocks are in steady state (we have used  $\gamma = 5/3$ ). The temperature ratio across the shock

$$\frac{T_2}{T_1} = \frac{1}{r} \left[ 1 + \frac{5}{3}M_1 \left( \sqrt{1 + 4M_1^2/9} + 2M_1/3 \right) \right] \quad , \quad (12)$$

depends on  $\beta_0$  and  $\Delta\theta$  through eqs. (10) and (11); this dependence is plotted in Figure 13.

## 4.2. Alternative reconnection models

In the discussion above the heating follows from non-resistive, post-reconnection dynamics alone. It is therefore natural that the model of LGL09 gives results similar to other

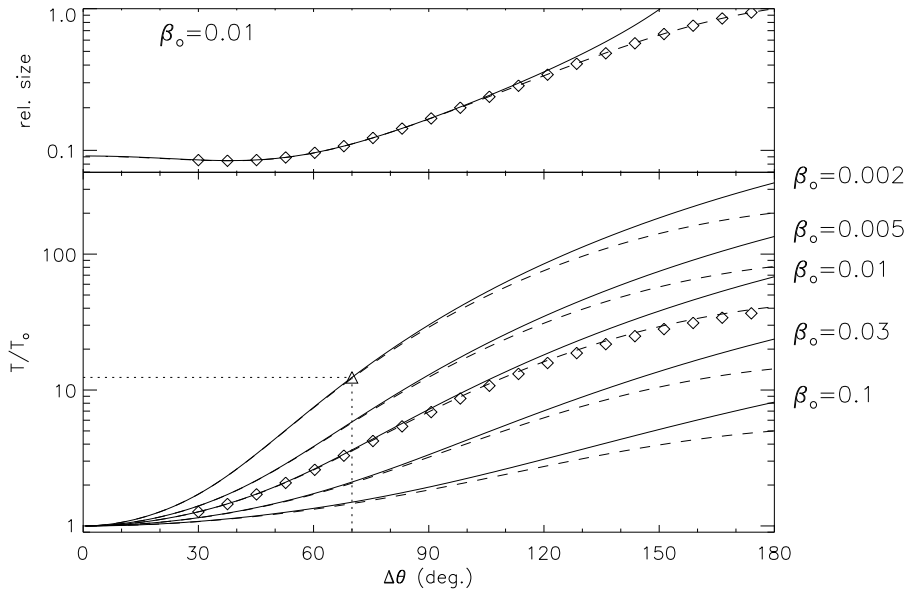


Fig. 13.— Properties of the PSP *vs.* the reconnection angle  $\Delta\theta$  for various models. Curves shown are solid: Longcope *et al.* (LGL09), dashed: Soward (1982) and diamonds: Lin and Lee (1994). The lower panel shows the temperature ratio,  $T_2/T_1$ , for various values of the initial plasma- $\beta$ , noted on the right. All models agree for small angles for each value of  $\beta_0$ . A triangle denotes the situation for a current sheet with  $\Delta\theta = 70^\circ$  and  $\beta_0 = 0.002$ . The top panel shows the fraction of the tube between RDs occupied by the PSP for the case of  $\beta_0 = 0.01$  for all three models.

models of fast magnetic reconnection. The most well-known such model, that of Petschek (1964), is of two-dimensional, steady-state reconnection between perfectly anti-parallel field:  $\Delta\theta = 180^\circ$ . In that model two long steady outflow jets are confined between standing SMSs. It was realized early on Petschek and Thorne (1967) that the addition of a guide field demanded a more complicated shock structure involving both RDs and SMSs. For  $\beta \approx 1$ , or  $\Delta\theta \simeq 180^\circ$ , the shocks are close together and the configuration appears similar to the classic Petschek one. In other cases, such as our own with  $\beta \ll 1$  and a significant departure from  $\Delta\theta = 180^\circ$ , the SMSs occur well inside the bends in the field: the RDs. From the conventional end-on perspective the configuration still resembles the Petschek model, but from the side-view perspective any given field line looks like the flux tube in the center panel of Figure 12 but with SMSs instead of GDSs.

A complete quantitative treatment of Petschek reconnection in the presence of a guide field was presented by Soward (1982) and then re-derived in simpler form by Forbes *et al.* (1989) and Vrsnak and Skender (2005). This analysis reveals that the post-reconnection temperature depends on angle and Alfvén speed alone, in a manner very similar to the transient three-dimensional LGL09 model (see Figure 13). It does not, for example, depend on the reconnection rate or even the microphysics generating the reconnection electric field. The distance along a given field line between the SMSs is some fraction of the distance between the RDs. In the steady-state, two-dimensional model this fraction depends on  $\Delta\theta$  in exactly the same way as the post-shock plasma (PSP) size does in the transient three-dimensional model (see top panel of Figure 13).

Properties of the more extensively studied Petschek model can be read off the far right side of Figure 13:  $\Delta\theta = 180^\circ$ . In that case the two shocks, RD and SMS, combine into the single shock with no gap — the PSP occupies 100% of the region, where the dashed curve intersects the right axis of the upper panel. The final temperature ratio depends on  $\beta_0$ ; the oft-used value  $\beta_0 = 0.01$  produces a 40-fold increase in temperature, in agreement with the dashed curve in the lower panel.

Figure 13 reveals remarkably good quantitative agreement, especially for  $\Delta\theta \lesssim 120^\circ$ , between seemingly different reconnection models. The level of disagreement at large angles results from significant reduction in field strength across the SMSs assumed absent from the GDSs of LGL09. This reduction drives the post-shock  $\beta$  to non-negligible values contradicting the assumption of LGL09 that  $\beta \ll 1$  on both sides. These assumptions do, however, appear to be good ones for smaller angles. In particular, the SMSs do not significantly decrease the magnetic field strength when  $\Delta\theta \lesssim 120^\circ$ , in contrast to their switch-off character in the traditional Petschek limit ( $\Delta\theta = 180^\circ$ ).

The agreement between a steady two-dimensional model and a non-steady three-dimensional

model can be understood in terms of a non-steady one-dimensional model. Lin and Lee (1994) solved the Riemann problem beginning with an infinite current sheet bending an otherwise uniform magnetic field. This sheet decomposes into a pair of fast magnetosonic rarefaction waves, outside a pair of RDs, outside a pair of SMSs. It has been demonstrated that this solution is similar to Petschek reconnection in two-dimensions either with or without a guide field Lin and Lee (1999). The diamonds in Figure 13 show that the SMS separation (relative to the RD separation) and the post shock temperature match those of Soward (1982) over all angles. Even a steady, magnetized flow contains individual flux tubes each undergoing time-dependent evolution. This evolution obeys non-resistive MHD, independent of the reconnection mechanism. Evidently it is equally well described in one, two or three dimensions.

We conclude that post-shock temperatures from fast reconnection across a current sheet depends on the field strength and angle according to a fairly robust relationship given by eq. (12) and shown in Figure 13. The specific details of the reconnection appear to be irrelevant in determining this particular property. The reconnection outflow may take the form of a long jet, as many models have assumed, or it may consist of numerous isolated plugs. Either situation produce very similar post-shock properties. For the initial angle  $\Delta\theta = 70^\circ$  to heat a plasma from active region temperature,  $T_0 = 3$  MK, to  $T_2 = 37$  MK observed in the loop-top source, requires reconnection at  $\beta_0 \simeq 0.002$ . In a field strength of  $B = B_g / \cos(35^\circ) = 400$  G, a 3 MK has this value of beta for  $n_{e,0} = 1.5 \times 10^{10} \text{ cm}^{-3}$ .

## 5. A Model of the Loop-top Source

We suggest that the loop-top thermal emission observed by RHESSI is from a post-shock plasma of the kind just described. The numerous distinct loops observed in  $171\text{\AA}$  suggest a spatially intermittent (patchy) reconnection has formed isolated high-temperature plugs of the kind shown in Figure 12. The flux tubes would be formed by reconnection across a current sheet like that in Figure 10. Each plug has the same cross-sectional area as the tube and extends a distance  $w(t)$  along its axis, as in Figure 12. With flux  $\delta\varphi$  and field strength,  $B$ , set by the flux layers between which it is confined, the flux tube has cross sectional area  $\delta\varphi/B$ . This is independent of the actual thickness of the current sheet across which the reconnection occurs; in fact the LGL09 model and the simulation which motivated it Linton and Longcope (2006); Linton, Devore, and Longcope (2009) take the sheet to much thinner than the tube. The emission measure of this one plug is

$$\delta EM = n_{e,2}^2 w \delta\varphi / B \quad , \quad (13)$$

where  $n_{e,2}$  is the post-shock electron density. Provided the plasma is sufficiently dense to thermalize, all of the plug’s emission is characterized by the post-shock temperature  $T_2$ .

New patches of reconnection, distributed over the current sheet, will produce new flux tubes, two per patch, at an average rate  $2\dot{\Phi}/\delta\varphi$ . Each of these includes a central plug which emits for a time  $\tau_{\text{plug}}$ . Emitting plugs have a combined emission measure

$$EM = 2n_{e,2}^2 \langle w \rangle \tau_{\text{plug}} \frac{\dot{\Phi}}{B_0} . \quad (14)$$

where  $\langle w \rangle$  is the axial extent averaged over the emitting life-time. The emission measure therefore depends, through properties on the right hand side, on the angle  $\Delta\theta$  between reconnecting field lines and the mean reconnection rate. This rate,  $\dot{\Phi}$  is not related to the reconnection electric field within a single patch, but is rather the rate at which new patches are produced throughout the current sheet.

### 5.1. The size and life of the PSP plug

The post-shock plasma (PSP) plug is confined by supersonic inflows generated by the rotational discontinuities (RDs) shown in Figure 12. The size,  $\langle w \rangle$  and life,  $\tau_{\text{plug}}$ , of a single emitting plug can be estimated by considering how long these flows are able to confine it. This follows from a detailed analysis of the plasma dynamics inside the retracting flux tube shown in Figure 12.

We hereafter assume reconnection at sufficiently low  $\beta_0$  (pre-reconnection) and at sufficiently large angle,  $\Delta\theta$ , that the flow in region 1 is hypersonic:  $M_1 \gg 1$  according to eq. (10). Using this in eq. (11) gives density ratio near the gas-dynamic limit  $r \simeq 4$ . We hereafter use this value to simplify the analysis; using the full expression would produce more complex expressions but similar values. The accretion of the inward flows cause the PSP to grow as the GDSs propagate at

$$v_s = \frac{v_{x,1}}{r-1} \simeq \frac{1}{3}v_{x,1} . \quad (15)$$

Vertical motion of the tube segment persists at roughly constant speed,  $v_{z,1} = -v_{A,0} \sin(\Delta\theta/2)$ , until it reaches the bottom of the current sheet. This happens at  $t_h = h/|v_{z,1}|$  (see Figure 12), at which time the PSP occupies

$$w(t_h) = 2v_s t_h = \frac{2}{3}h \tan(\Delta\theta/4) , \quad (16)$$

of the total segment length,  $2h \cot(\Delta\theta/2)$ . This is the fraction whose dependence on  $\Delta\theta$  is plotted in Figure 13. In purely two-dimensional models, *i.e.*  $\Delta\theta = 180^\circ$ , the retraction is

halted at a fast magnetosonic termination shock Forbes and Priest (1983); here it is a single event in the evolution of the tube and the PSP.

The end of the RDs means the end of the supersonic inflows confining the PSP. The vertical forces which halt the retraction do not, however, directly stop the horizontal flow throughout region 1. Instead, inflow stoppage propagates horizontally as a rarefaction wave (RW<sub>1</sub> in Figure 14) moving at  $v_f = c_{s,1} + v_{x,1} \simeq v_{x,1}$ . At time  $t_h$  the rarefaction wave and the shock are separated by a horizontal distance

$$\Delta x = h \cot(\Delta\theta/2) - \frac{1}{2}w(t_h) = h[\cot(\Delta\theta/2) - \frac{1}{3}\tan(\Delta\theta/4)] \quad , \quad (17)$$

as shown in Figure 14. They move toward one another at relative speed,  $v_f + v_s$ , meeting after

$$\Delta t_f = \frac{\Delta x}{v_{x,1} + v_s} = \frac{h}{4v_{x,1}} [3 \cot(\Delta\theta/2) - \tan(\Delta\theta/4)] \quad . \quad (18)$$

At this time the shock has propagated a horizontal distance

$$w_{\max} = 2v_s(t_h + \Delta t_f) = \frac{h}{2 \sin(\Delta\theta/2)} \quad (19)$$

since the reconnection episode; this is the maximum extent of the plug (see Figure 14).

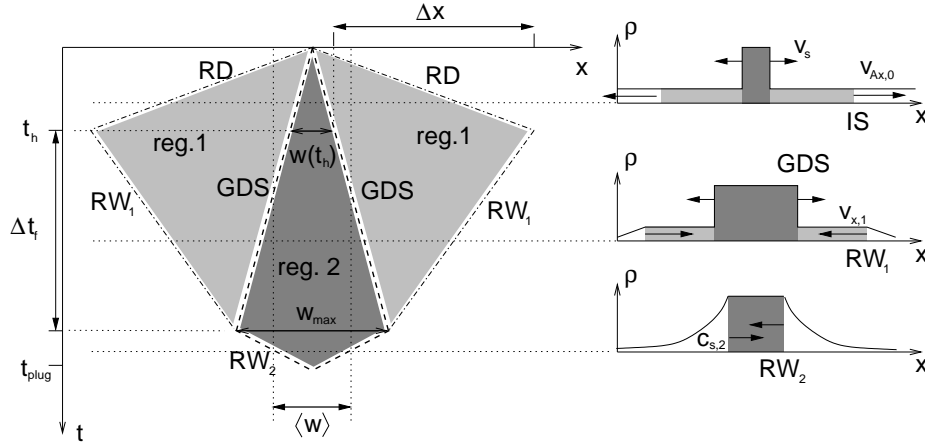


Fig. 14.— A schematic of the time evolution of the post-shock plasma plug depicted with time running downward. The three graphs on the right show density  $\rho$  vs.  $x$  at characteristic times. Regions 1 and 2 are light and dark grey regions confined by shocks and rarefaction waves moving at different horizontal velocities. The panel on the left shows the evolution of these regions and the different shocks. Horizontal arrows show the extent of the PSP plug at specific times.

The interaction of the rarefaction wave and the gas-dynamic shock results in a new rarefaction wave (RW<sub>2</sub>) propagating toward the center of the plug at the post-shock sound

speed  $c_{s,2}$ . This represents the free expansion of the unconfined hot plasma which ultimately disassembles the plug. These second rarefaction waves will meet after an interval

$$\Delta t_c = \frac{w_{\max}}{2c_{s,2}} = \frac{w_{\max}}{2v_{x,1}} M_1 \sqrt{\frac{T_1}{T_2}} = \frac{w_{\max}}{v_{x,1}} \frac{3}{2\sqrt{5}} , \quad (20)$$

marking the end of the PSP. The final expression in eq. (20) uses the high Mach-number limit of eq. (12),  $T_2/T_1 \rightarrow (5/9)M_1^2$ . The total lifetime of the plug

$$\tau_{\text{plug}} = \frac{1}{2}w_{\max} \left[ \frac{1}{v_s} + \frac{1}{c_{s,2}} \right] = \frac{3w_{\max}}{4v_{A,0} \sin^2(\Delta\theta/4)} \left[ 1 + \frac{1}{\sqrt{5}} \right] , \quad (21)$$

is longer than its free expansion by a factor  $c_{s,2}/v_s \simeq \sqrt{5}$ . Since the plug expands linearly and then contracts linearly its average extent is one-half its maximum:

$$\langle w \rangle = \frac{1}{2}w_{\max} = \frac{h}{4 \sin(\Delta\theta/2)} \quad (22)$$

In the analysis above the life time of the emitting plasma was fixed by the time-scale for pressure confinement. Several previous investigations have used instead a time-scale for dissipation by conductive cooling Jiang *et al.* (2006). A detailed analysis by Guidoni and Longcope (2010) shows that conductivity produces extended thermal fronts in advance of the GDSs. Temperature increases gradually over the fronts reaching the steady-state Rankine-Hugoniot value at the density jump which is the actual GDS (Kennel 1987; Xu and Forbes 1992; Guidoni and Longcope 2010, more accurately called an iso-thermal sub-shock). There is very little density enhancement within the fronts, so they would not contribute appreciably to the emission measure. Thermal conduction could precede the rarefaction wave  $RW_2$ , causing  $\Delta t_c$  to be even smaller than our estimate in eq. (20). This is the smallest contribution to  $\tau_{\text{plug}}$  so we expect that eq. (21), based on pressure confinement alone, is probably close to the actual life.

## 5.2. The loop-top emission

Assuming the reconnection occurs near the center line of the current sheet, of width  $\Delta$ , the net retraction distance is  $h = \Delta/2$ . The current sheet width is related to the reconnection angle by eq. (8),

$$h = \frac{B_g}{B'_\perp} \tan(\Delta\theta/2) , \quad (23)$$

from the structure of the Green-Syrovaetskii sheet with a guide field. The field properties at the separator point in Figure 10 and an angle  $\Delta\theta = 70^\circ$  inferred from RHESSI temperatures

gives an average plug size of  $\langle w \rangle = 3.0$  Mm. Taking the external density to be  $n_{e,0} = 1.5 \times 10^{10} \text{ cm}^{-3}$  gives a life-time of  $\tau_{\text{plug}} = 8.5$  sec. The loop-top source is somewhat larger and considerably longer-lived than a single PSP so it must consist of many such events at any one time.

The net emission measure from the assembly of plugs is given by eq. (14). Expressing the total magnetic field in terms of the guide field,  $B_0 = B_g / \cos(\Delta\theta/2)$ , and using eq. (23), gives

$$EM = 15.4 \frac{n_{e,0}^{5/2} \sqrt{m_p}}{B_{\perp}^2} \frac{\dot{\Phi}}{\sin^2(\Delta\theta/4)} , \quad (24)$$

where  $m_p = \rho/n_e$  is the proton mass. In this way the emission measure in super-hot thermal material is directly proportional the rate of reconnection.

There are several ways by which we might derive the reconnection rate  $\dot{\Phi}$ . Equations (3), (5) and (8), concerning the Green-Syrovatskii current sheet, can be combined to yield a relation between flux transfer and the decrease in reconnection angle

$$\dot{\Phi} = - \frac{d|\Delta\Psi|}{dt} = - \pi L \frac{B_g^2}{B_{\perp}'} \frac{\sin(\Delta\theta/2)}{\cos^3(\Delta\theta/2)} \frac{d(\Delta\theta)}{dt} . \quad (25)$$

The reconnection angle  $\Delta\theta$  decreases as the current decreases due to reconnective flux transfer across the sheet. The temperature of the PSP also depends on  $\Delta\theta$  as shown in Figure 13. It is the decrease in this angle, due to reconnection, which leads to the decreasing temperature in the super-hot thermal component shown in Figure 9. We can combine these two relations to derive  $\Delta\theta(t)$  from  $T(t)$  for  $B_g = 331\text{G}$  and an assumed value of pre-reconnection density,  $n_{e,0}$ .

Assuming larger densities  $n_{e,0} = 3 - 8 \times 10^{10}$  results in slightly larger reconnection angles  $\Delta\theta = 80^\circ - 100^\circ$  due to larger  $\beta_0$ . The decreasing temperature causes the angle to decrease at  $-\Delta\theta/dt \simeq 65$  degrees per hour for the two density choices. Using these rates and angles in eq. (25) leads to  $\dot{\Phi} \simeq 20 - 50$  Gigavolts as shown in Figure 15. This flux transfer rate in eq. (24) gives an emission measure commensurate with RHESSI observations when the larger initial density,  $n_{e,0} = 8 \times 10^{10} \text{ cm}^{-3}$  is used.

A more direct, and more conventional, measurement of  $\dot{\Phi}$  can be obtained by mapping the apparent motion of flare ribbons across the magnetic field in the lower atmosphere Forbes and Priest (1984); Poletto and Kopp (1986). This is frequently done with high cadence TRACE UV (1600Å) images Saba, Gaeng, and Tarbell (2006); Longcope *et al.* (2007), but these were unavailable at this time since TRACE was imaging instead in EUV 171 Å. Observations at this wavelength usually reflect  $\geq 1$  MK plasmas in the corona, however, the bandpass does include contribution by enhanced chromospheric emission at the feet of flare

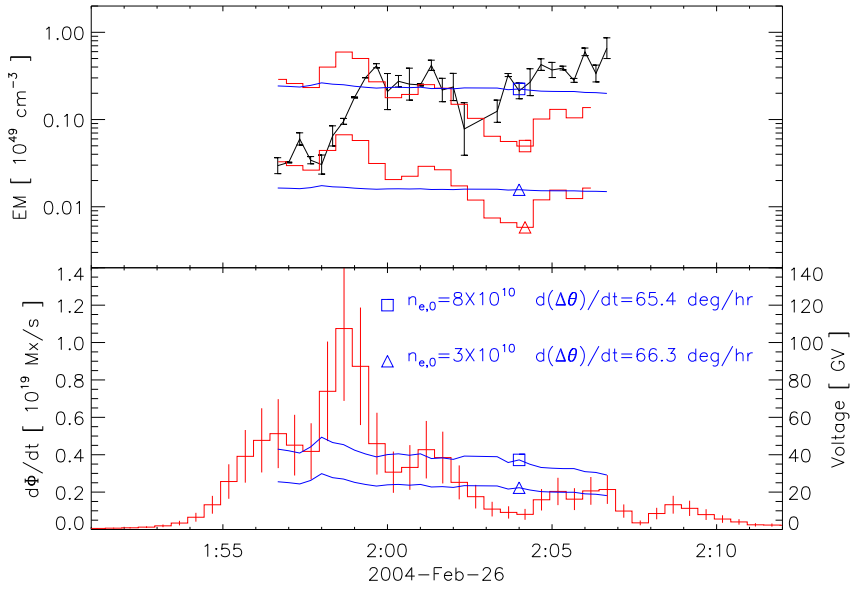


Fig. 15.— Plots of inferred flux transfer rates (bottom) and the emission measure they would produce. Blue curves are derived from the temperature change using eq. (25) and red curves are from the motion of  $171\text{\AA}$  ribbon features across the magnetogram. Curves with triangles (squares) are derived using  $n_{e,0} = 3 \times 10^{10} \text{ cm}^{-3}$  ( $n_{e,0} = 8 \times 10^{10} \text{ cm}^{-3}$ ). The black curves are the super-hot emission measure derived from RHESSI, error bars are the values from detectors 3 and 4 alone.

loops especially in the early phase of the flare. Such emission is evident in the 1:59:14 and 2:03:14 panels of Figure 4.

We therefore use 171Å images to compute the reconnection flux transfer rate. We outline the chromospheric ribbons seen at the start of the flare, and, as the flare evolves, track only the outward spread of the ribbon, *i.e.* the spread of the brightening away from the polarity inversion line. This approach avoids contamination due to emission by multi-megakelvin plasmas in the post-flare loops, which have cooled down to emit in 171Å between the expanding ribbons.

The flare ribbons are tracked in co-aligned TRACE 171 Å images from 1:00 UT for two hours with a cadence of approximately 40 s and a pixel scale of 0.5 ″. The chromospheric ribbons are then mapped in a magnetogram co-aligned with the flare images and the total magnetic flux covered by the ribbons is measured. To approximate the magnetic field in the chromosphere, we extrapolate the photospheric line-of-sight magnetic field, obtained by MDI/SoHO 20 minutes before the flare onset, into a nominal chromosphere height of 2000 km using a potential field assumption. Numerous experiments have shown that measurement of the reconnection flux is quite robust Qiu *et al.* (2007). The extrapolation merely decreases the measured reconnection flux by 25%, but does not modify the time profile of  $\dot{\Phi}$ . Assumptions other than a potential field assumption (such as a linear-force-free assumption) and/or extrapolation to a different height  $\leq 2000$  km would not change the  $\dot{\Phi}$  profile, and its magnitude would be modified by  $\leq 25\%$ .

We also estimate uncertainties in the flux measurement by mis-aligning MDI magnetogram and TRACE images by up to 2″ and by using a set of brightness threshold values for ribbon detection. The upper-limit of the uncertainty due to these sources is 30%. Given the geometry of this flare, the flare ribbon in the negative magnetic field is more accurately tracked. Therefore  $\dot{\Phi}$  measured in the negative field is used and plotted in red on Figure 15. Using this rate in eq. (25) gives independent measures of the super-hot emission measure. Once again we find agreement when the larger initial density,  $n_{e,0} = 8 \times 10^{10} \text{ cm}^{-3}$  is used.

Relation (25) could be inverted to use the observed super-hot emission measure to estimate  $\dot{\Phi}$ . Agreement in Figure 15 shows that doing so yields a third independent measure in agreement with the other two – temperature decrease and ribbon motion. It appears that the flare is driven by flux transfer at a mean rate  $\dot{\Phi} \approx 4 \times 10^{18} \text{ Mx/s}$  (40 Gigavolts). We stress once more that this is not a local electric field, but rather the net effect of multiple reconnection events.

## 6. A Model of the flare

### 6.1. The loop-top source

The TRACE loops appearing in the 171Å images (i.e Figure 4) have typical diameters of 2 Mm. Attributing to them the same field strength as the separator,  $B \approx 330$  G, means each has flux  $\delta\varphi = 10^{19}$  Mx. Patchy reconnection at the inferred rate,  $\dot{\Phi} = 4 \times 10^{18}$  Mx sec<sup>-1</sup>, would produce such flux tubes at the rate of  $2\dot{\Phi}/\delta\varphi = 1$  per second. The PSP plug at the center of each tube would persist for  $\tau_{\text{plug}} \simeq 8$  sec, so there would be  $\approx 8$  such plugs visible at any time. Using the  $\Delta\theta = 100^\circ$  angle inferred from the emission measure computations means the plugs are confined between  $|\mathbf{B}| = 430$  G field, and are thus 1.7 Mm in diameter; they range in length from zero to  $w_{\text{max}} = 5$  Mm. We posit that the  $9 \times 16$  Mm loop-top source in the 25 – 50 keV RHESSI images (Figure 8b – c) is such a superposition of plugs. While 8 plugs are visible at any instant, each image shows a super-position of  $\approx 28$  plugs visible for some portion of its 20-second integration (see Figure 16).

The volume of a super-hot plug would average  $\langle w \rangle \delta\phi / B \simeq 5 \times 10^{24}$  cm<sup>3</sup>, so the combined volumes of the 8 plugs simultaneously visible at one instant is  $V = 4 \times 10^{25}$  cm<sup>3</sup>. Assigning to the observed loop-top source a volume  $V_s = \pi(4.5 \text{ Mm})^2(16 \text{ Mm}) = 10^{27}$  cm<sup>3</sup>, as estimated by the 70% contour of 25 – 50 keV images in Figure 16, it would have a filling factor of  $f = 0.04$ . (Had we used the 50% contour instead, the filling factor would have been  $f = 0.01$ .) A post-shock density of  $n_{e,2} = 4n_{e,1} = 3 \times 10^{11}$  cm<sup>-3</sup> gives the ensemble of plugs an emission measure of  $EM = 4 \times 10^{48}$  cm<sup>-3</sup>, in good agreement with Figures 9 or 15.

Transferring the entire domain flux,  $\Delta\Psi_{4-1} = 2.8 \times 10^{21}$  Mx, would take  $\tau_{\text{TX}} \simeq 12$  minutes at a steady reconnection rate  $\dot{\Phi} = 4 \times 10^{18}$  Mx sec<sup>-1</sup> inferred above. Each reconnection event transfers flux  $\delta\phi = 10^{19}$  creating two post-reconnection loops — one in each post-reconnection domain. Thus we expect  $\approx 560$  flux tubes will be created over  $\approx 700$  seconds (12 minutes). It is this transfer rate, rather than cooling following impulsive heating, that sets the overall flare time scale.

### 6.2. Post-flare loops

We have presented a model for how fast reconnection could produce super-hot plasma just outside the diffusion region. One plug of this super-hot plasma would persist for  $\tau_{\text{plug}} \simeq 8$  seconds before the confining flows cease and its own high pressure caused its disassembly. Thermal conduction during and following the plug’s compression would eventually reach the footpoints of the flux tube causing evaporation. Details of this phase are beyond the scope

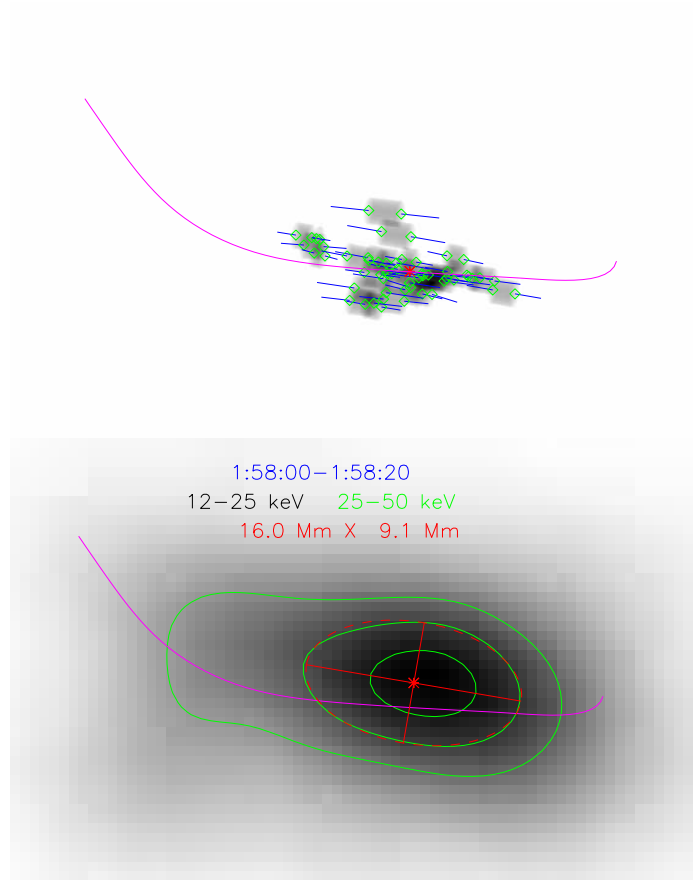


Fig. 16.— Images of the loop-top source. (top) A super-position of 28 plugs 2 Mm across with lengths varying randomly to 6 Mm. They are distributed randomly in space near the separator (magenta curve). Blue lines show the extent of the RD along the field lines, and green diamonds show the locations of the GDSs. A red asterisk marks the centroid of the super-position. (bottom) RHESSI images from 12 – 25 keV (inverse grey scale) and 25–50 keV (green contours) from an integral over 1:58:00 – 1:58:20, at the peak of the thermal phase. The red curves show an ellipse with moments matching the central (70%) contour of the 25–50 keV emission. The major and minor axes, 16.0 Mm and 9.1 Mm, are straight lines.

of our model, however, it is possible to predict its overall contribution.

We suggest that the evaporation from the thermal conduction fills the loop with lower-temperature plasma observed as the cooler ( $T \simeq 20$  MK) component of the RHESSI spectra. Following Antiochos and Sturrock (1978) we assume the conductive cooling transfers all energy from the thermal and kinetic energy of the tube to the evaporated component. The temperature and emission measure of this component matches the plasma observed in X-rays by GOES (see Figure 9). Such observations are commonly explained in terms of the Neupert effect Neupert (1968); Dennis and Zarro (1993) whereby direct flare energy release evaporates chromospheric material. We propose here that, at least in this present case, the evaporation is driven by thermal conduction rather than non-thermal particles.

Images from RHESSI’s 6 – 12 keV often resemble other soft-ray images and can be used to estimate the extent of the plasma detected by GOES. The 50% red contours Figures 8a – d outlines a  $30 \times 16$  Mm region, suggesting an ellipsoid of volume  $V = 4 \times 10^{27}$  cm<sup>3</sup>. Using a filling factor,  $f = 0.18$ , justified below, we estimate the density of evaporated material as  $n_e = \sqrt{EM/fV}$ . Using  $EM$  from ratio of GOES channels gives a maximum  $n_e = 2.6 \times 10^{11}$  cm<sup>-3</sup> at 2:04:12, thereafter falling steadily to  $n_e = 6 \times 10^{10}$  at 3:00:00.

Once a fully retracted tube is full of  $T \approx 20$  MK plasma from evaporation it will cool through thermal conduction and then radiation. According to the cooling model of Cargill *et al.* (1995), a loop at the temperature and density inferred from GOES, and length given by eq. (1), would cool to half its temperature in between 1 minute (at 1:58) and 3 minutes (at 2:30). They would reach  $T \simeq 1$  MK shortly thereafter and appear in the TRACE image. This explains loops visible by TRACE almost immediately, even as the temperature inferred by GOES approaches 1 MK much more gradually. The continued appearance of the these loops over one hour is due to the continued creation of new loops through reconnection.

### 6.3. Energetics

Each tube of reconnected flux  $\delta\phi = 10^{19}$  Mx releases energy by decreasing its length by a distance  $\Delta\ell = 2h \tan(\Delta\theta/4)$ . This decrease in length, with no appreciable change in field strength, will decrease the flux tube’s magnetic energy by

$$\delta E = \frac{B\delta\phi}{8\pi}\Delta\ell \simeq 10^{29} \text{ erg} \quad , \quad (26)$$

using values inferred for the current sheet, with  $h = 7$  Mm and  $\Delta\theta = 100^\circ$ ,  $B = 430$  G. The expansion of the external flux layers into the volume vacated by the retraction will release an equal amount of energy (LGL09) leading to a net release of  $\delta E_{\text{mag}} = 2 \times 10^{29}$  ergs. This is

the value at the onset of the flare (1:58:00); later flux tubes will release steadily diminishing energies as the current sheet shrinks causing  $\Delta\theta$  and  $h$  to decrease. If the average energy release is half the maximum value, the complete set of 560 flux tubes would release  $5.6 \times 10^{31}$  ergs, consistent with the initial free energy,  $\Delta W$ , from eq. (6).

At a time  $t_h = 3$  sec following its reconnection a given tube has fully retracted and released all its magnetic energy. At this instant the plug is  $w(t_h) = 2.2$  Mm long and contains thermal energy

$$U_{\text{th}}^{(\text{plug})}(t_h) = 3k_b T_2 n_{e,2} (\delta\phi/B) w(t_h) \simeq 2 \times 10^{28} \text{ ergs} \quad (27)$$

only 10% of the magnetic energy liberated by the reconnection,  $\delta E_{\text{mag}}$ . This is rather low efficiency compared to the anti-parallel case ( $\Delta\theta = 180^\circ$ ) where 40% of the free energy is directly thermalized by the slow shocks Priest and Forbes (2000). In our case the other 90% of the liberated energy was converted into bulk kinetic energy of retraction. Roughly one-sixth ( $\sin^2[\Delta\theta/4]$ ) of that remaining kinetic energy is directed horizontally and is ultimately thermalized before the plug disassembles itself. Thus 25% of all magnetic energy liberated by reconnection appears as thermal energy in the loop-top source at some point. Since a given plug will have, on average, half of this amount at a random time, the eight plugs simultaneously visible will contain

$$U_{\text{th}}^{(\text{sh})} = 8 \times 3k_b T_2 n_{e,2} (\delta\phi/B) \langle w \rangle \simeq 10^{29} \text{ erg} . \quad (28)$$

This is our estimate of the thermal energy contained in the super-hot loop-top source at its peak.

The instantaneous thermal energy content of the low-temperature component, filled with evaporated material, is  $U_{\text{th}}^{(\text{GOES})} = 3k_b T \sqrt{EMVf}$ , where we take  $T$  and  $EM$  from the GOES channels and assume a filling factor  $f = 0.18$  for reasons described below. The thermal energy, shown in Figure 17, rises to a peak of  $2 \times 10^{30}$  ergs at 2:01:25. At 1:58:00, when we found the super-hot component energy, the low-temperature component has an order of magnitude more (red triangle).

The low-temperature component cools by radiation and by thermal conduction. Radiative losses, computed using the temperature dependent Mewe radiative loss function Mewe, Gronenschild, and van den Oord (1985), are plotted in blue on Figure 17. The rate of conductive energy loss to the chromosphere is  $P_{\text{cond}} = U_{\text{th}}/\tau_{\text{cond}}$  where

$$\frac{1}{\tau_{\text{cond}}} = \frac{\kappa |\nabla T|}{3k_b T n_e (L/2)} \simeq \frac{\kappa_0 T^{5/2}}{3k_b n_e (L/2)^2} , \quad (29)$$

for a loop of full length  $L$ ; Spitzer conductivity is  $\kappa = \kappa_0 T^{5/2}$ . The EUV loops traced in Figure 5 had apparent (plane-of-the-sky) lengths increasing from 7 Mm to 12 Mm according to

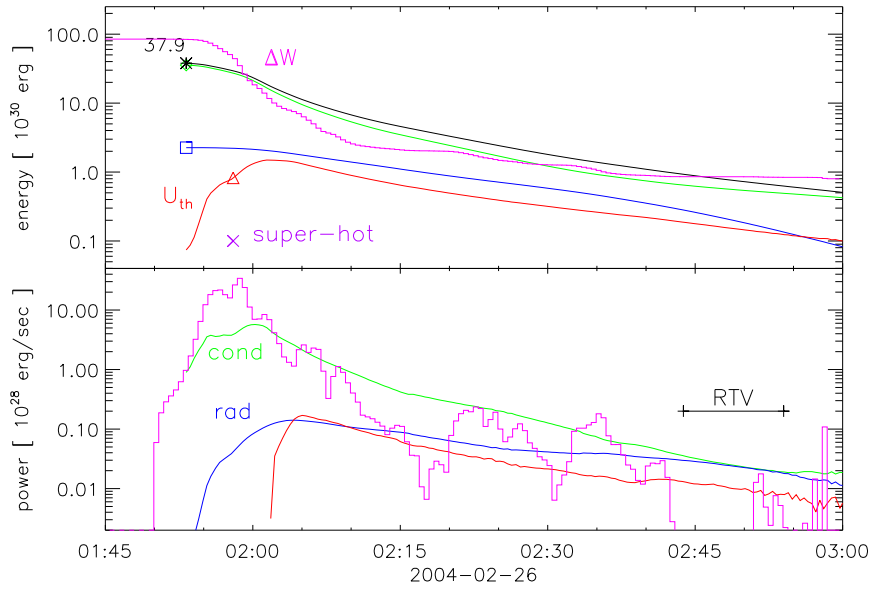


Fig. 17.— Time histories of the energy (top) and power (bottom) from the flare. Green and blue curves are losses from conductivity and radiation respectively. These losses are integrated backward to produce cumulative energies in the top panel — the net energy lost *after* that time. The red line in the top panel is the thermal energy content,  $U_{\text{th}}^{(\text{sh})}$  from eq. (28), in the lower panel it is  $-dU_{\text{th}}^{(\text{sh})}/dt$ . The instantaneous thermal energy content of the low-temperature and high-temperature components at 1:58:00 are shown in the top panel by  $\diamond$  and  $\times$  respectively.

empirical relation eq. (1). Doubling this time-dependent function to account, approximately, for the third dimensions and portions not observed at  $171 \text{ \AA}$  gives conductive cooling times ranging from  $\tau_{\text{cond}} = 10 \text{ sec}$  at 2:00, to  $\tau_{\text{cond}} = 280 \text{ sec}$  at 3:00. The resulting conductive losses are plotted in Figure 17. These losses actually represent a transfer of energy to the lower temperature atmosphere, where it is presumably radiated. This radiative loss is known to far exceed the radiation from optically thin coronal plasma inferred from the GOES X-ray bands Emslie *et al.* (2005). We use the conductive losses to approximately quantify this other loss mechanism.

At  $T \simeq 20 \text{ MK}$  conductive losses dominate radiative losses by up to an order of magnitude. We chose filling factor  $f = 0.18$  in order that the two become equal at late times, designated RTV in Figure 17, as they should be in a static equilibrium Rosner, Tucker, and Vaiana (1978). Prior to that, short conductive cooling times, 10 – 280 seconds, demand a sequence of new, dynamic loops Warren, Winebarger, and Hamilton (2002); Warren (2006).

Integrating each of the losses gives the cumulative losses shown in the top panel of Figure 17. The total integrals of radiation and conduction,  $2.3 \times 10^{30}$  ergs and  $3.3 \times 10^{31}$  ergs, are shown by a square and diamond, respectively. We estimate the total energy lost by the low energy component as the sum of these two  $\Delta W = 3.8 \times 10^{31}$  (asterisk). This is a slightly smaller than the MCC estimate of free magnetic energy, eq. (6), suggesting, among other possibilities, incomplete magnetic relaxation.

To ascertain the degree of reconnection we integrate the ribbon-swept flux whose change,  $\dot{\Phi}$  is plotted Figure 15. The flux discrepancy

$$\Delta\Psi(t) = \int_t^\infty \dot{\Phi}(t') dt' \quad , \quad (30)$$

is the same as the ribbon flux, but accumulated from the final time. The initial value of this flux,  $\Delta\Psi = 3.3 \times 10^{21} \text{ Mx}$ , is 20% larger than  $\Delta\Psi_{4-1}$ . The later is only a single post-reconnection domain, albeit the largest one, so it is perhaps unsurprising that it falls short of the total flux swept by the flare ribbons. Using the ribbon-swept flux in the magnetic energy estimate, eq. (6), with the same separator  $L = 54 \text{ Mm}$ , gives an estimate of the magnetic energy liberated by reconnection. The total,  $\Delta W = 8.5 \times 10^{31}$  ergs, half-again as large as the estimate using  $\Delta\Psi_{4-1}$  and twice the energy released by the flare. Indeed, throughout the thermal phase of the flare, after 1:56:40, the free magnetic energy tracks the total flare energy very well. It seems that energy release through magnetic reconnection is a viable candidate for producing the observed flare emission.

## 7. Discussion

We have presented here a new model for the shock heating of plasma as magnetic energy is released following magnetic reconnection. The flux transfer achieved by the reconnection electric field *triggers* this energy release but does not directly participate in it. As a result its details do not enter the prediction, and we have bypassed their consideration. The model presented here applies a novel treatment of transient, localized reconnection in three dimensions, but its shock heating is closely related to the traditional two-dimensional, steady-state model of Petschek. The role of shocks are similar in both cases, but the former does not occur in an out-flow jet geometry.

We have applied this model to RHESSI, TRACE, MDI and GOES observations of a particular compact X-class flare. Magnetic energy is stored during a 50-hour emergence of flux within the active region, and then released by reconnection over less than one hour. The majority of energy released in the flare appears to occur through the production of a super-hot ( $T \gtrsim 30$  MK) thermal loop-top source, rather than through the acceleration of non-thermal particles. Our model predicts temperature and emission measure of the source, roughly consistent with those inferred from fitting the RHESSI spectra.

The observed source is modeled as a super-position of short-lived plugs of plasma heated and compressed by the post-reconnection shocks. While this ensemble never contains more than 1% of the magnetic energy ultimately released by the flare, it is the first stage in the entire energy release process. The subsequent expansion and conductive cooling of the plugs drives chromospheric evaporation to produce the more plentiful low-temperature plasma ( $T \lesssim 20$  MK) observed in soft X-rays. These cool freely to appear minutes later, when  $T \simeq 1$  MK, in TRACE EUV images. The numerous discrete loops are a direct consequence of the transient, localized reconnection which creates them; their early appearance is a result of the rapid, independent evolution of each loop. The smooth evolution of the ensemble is a result of the gradual decrease in current as flux is transferred.

We assumed the reconnection occurred within a current sheet which had formed at some time prior to the flare. Current sheets are pre-requisites for traditional fast reconnection models since they bring field lines of significantly different connectivity close enough to be mutually affected by a small-scale reconnection electric field. We estimated the properties of the current sheet assuming it be in equilibrium or reconnecting slowly according to the Sweet-Parker model. (Any possible resistive dissipation in this pre-flare current sheet is neglected in our energy-release scenario.) The two current sheet properties most significant for our model are the strength of the equilibrium magnetic field adjacent to it and the angle between the magnetic field it separates.

In addition to the magnetic properties, our model depends on the density of the flux tube plasma prior to its reconnection. This density determines both the Alfvén speed and the post-shock density. We found that large observed emission measures demand fairly large densities,  $n_{e,0} \approx 8 \times 10^{10} \text{ cm}^{-3}$ . This demand is not unique to our model, since it derives from the limit on density enhancement at a single shock. Indeed, our oblique shocks, similar to gas-dynamic shocks, produce a larger enhancement factor than switch-off shocks of two-dimensional models: 4 *versus* 2.5. It thus seems impossible that the super-hot post-shock material could have arisen from pre-shock material at densities comparable to those observed in non-flaring active regions,  $n_e \approx 10^9$ . Something in the flare process evidently “pre-fills” the flux — at least the flux immediately adjacent to the current sheet.

While the high post-shock density was inferred from the observed emission measure, independent evidence for it comes from the occurrence of thermal bremsstrahlung from a plasma at  $T \approx 40 \text{ MK}$  confined to  $\lesssim 10 \text{ Mm}$  along a magnetic field. The mean-free paths of electrons at that temperature,  $\ell_{\text{mfp}} = 100 \text{ Mm} (10^9/n_{e,2})$ , will greatly exceed the size of the source when density is low. Low density plasma streams accelerated by field line retraction (*i.e.* the RDs) would presumably pass through one another, rather than shocking. Such counter-streaming has been observed in simulations of collisionless fast reconnection Drake *et al.* (2009). The fact that we observe bremsstrahlung from a Maxwellian electron population implies sufficient collisionality to thermalize the loop-top source:  $\ell_{\text{mfp}} \lesssim 1 \text{ Mm}$ , and therefore very high post-shock density;  $n_{e,2} \gtrsim 10^{11} \text{ cm}^{-3}$ .

The pre-reconnection density  $n_{e,0}$  is not, strictly speaking, a pre-flare density. The thermal phase of the flare, to which our modeling has been devoted, began three minutes after the flare itself. We have no estimate of the coronal density, even post-reconnection, from the first three minutes (1:53:30 — 1:56:40) where thick-target emission was the best fit. It is entirely possible that the pre-flare density was far lower than the density we infer for flux tubes reconnected during the thermal phase of the flare. Indeed, all observational evidence suggests pre-flare densities typical of ARs:  $n_e \approx 10^9$ . One possibility for large  $n_{e,0}$  during that phase is that energy release during the initial non-thermal phase somehow enhanced the density of flux tubes in the vicinity of the current sheet *prior to* their reconnection.

We have not attempted to address the non-thermal phase with our purely fluid model, and therefore cannot include its energetic contribution in our estimate. It is over this period that the inferred magnetic energy input diverges most from the energy output in Figure 17. Our output rate neglects the precipitation of non-thermal particles, and uses conductive losses assuming collisional, Spitzer transport. We therefore expect the input and output to disagree to some extent during this period, as they do.

In contemplating possible sources of non-thermal particles it is worth recalling the failure

of fluid model when pre-reconnection densities are too low. Low collisionality in the post-shock density leads to a non-thermal electron population with mean free paths comparable to, or larger than, the total loop length. Furthermore, higher pre-reconnection Alfvén speeds lead to even higher post-shock temperature predictions,  $T_2 \approx v_{A,0}^2 \approx n_{e,0}^{-1}$ . While these extremely large temperatures could not be collisionally thermalized within the loop, they are based on energy conservation laws which must still obtain. We therefore expect a population of high energy, non-thermal electrons, accelerated directly by the Alfvénic loop retraction, the details of which awaits future kinetic calculations.

The above reasoning suggest that the non-thermal phase occurs when the pre-reconnection densities are low. The ambient, pre-reconnection densities rise, perhaps due to evaporation driven by observed precipitation of non-thermal particles, and subsequent reconnection occurs at densities high enough to produce collisionally thermalized plasma at the loop-top.

This evaporation scenario is similar to standard flare models except that ours requires evaporation to occur on a flux tube *before* that flux tube reconnects to release its energy. It is the rapid energy release that raises the temperature of the already-dense material to  $T \approx 40$  MK. Evaporation flow is unlikely to cross field lines so evaporative pre-filling seems to require a single flux tube to undergo multiple reconnections. In fact, models of reconnection in more complex magnetic topologies do predict a single flux tube to reconnect several times, passing through different separators into intermediate domains Longcope *et al.* (2007); Longcope and Beveridge (2007). Moreover, we observe post-flare loops (Figure 4) in domains, such as *P09 – N01*, before we observe them in *P04 – N01*, for which we compute the net flux transfer. Sufficient time between successive reconnections would permit a tube to be “pre-filled” by evaporation driven by energy released by this preceding reconnection.

The requirement that evaporation pre-fill loops before their final, energy-releasing reconnection, offers insight into the rarity of thermal flares of the kind we have modeled. Evaporative pre-filling is probably easier, and therefore a more common occurrence, in small compact flares, with short loops, than in large eruptive flares. The loops in this flare, ranging from  $L = 13 - 22$  Mm (doubling the visible EUV lengths in eq. [1]), are short compared to those in eruptive events. Furthermore, the reconnection was estimated to occur very low in the corona:  $\approx 10$  Mm. The emergence of new flux into this small active region appears to have loaded it with  $\Delta W \approx 10^{32}$  ergs, which was later liberated by reconnection. This produced short post-reconnection loops which were quickly filled even as they continued to be shortened.

Uncommon are flares whose energy release is sufficiently dominated by thermal emission to be modeled only as a fluid, however, we believe our energy release scenario may have broader applicability. Large eruptive flares often exhibit supra-arcade downflows,

which offer evidence for the same kind of post-reconnection retraction used in our model McKenzie and Hudson (1999); Sheeley, Warren, and Wang (2004); McKenzie and Savage (2009). Ultimately any kind of magnetic reconnection releases energy by permitting field lines to become shorter (except in the special case of anti-parallel fields, where some of the field energy is annihilated). If it is fast reconnection then the shortening will occur at the Alfvén speed, and plasma on the field lines will be compressed super-sonically. We therefore expect the energy release scenario in our model to be fairly common, although perhaps not always treatable by fluid models when densities are too low. Even in large, two-ribbon flares, however, the gradual phase shows little evidence of non-thermal particles and yet can account for substantial share of the energy release Emslie *et al.* (2005). Since it persists far longer than the cooling time of a single loop, the gradual phase must be maintained as a succession of new reconnection sites create and energize new loops Warren, Winebarger, and Hamilton (2002); Reeves and Warren (2002). The energy release in these cases may well occur through the same shock heating scenario introduced here, evidently without any non-thermal particles.

This work was supported under the NSF-REU program and by a joint NSF/-DOE grant. We thank Jim Drake, Terry Forbes, Jack Gosling, Silvina Guidoni, Mark Linton and Harry Warren for helpful discussions during the preparation of the manuscript. We also thank the anonymous referee for suggestions for improving the manuscript.

## REFERENCES

- Acton, L.W., Feldman, U., Bruner, M.E., Doschek, G.A., Hirayama, T., Hudson, H.S., Lemen, J.R., Ogawara, Y., Strong, K.T., Tsuneta, S.: 1992, *PASJ* **44**, L71.
- Antiochos, S.K., Sturrock, P.A.: 1978, *ApJ* **220**, 1137. doi:10.1086/155999.
- Aschwanden, M.J.: 2002, *Particle acceleration and kinematics in solar flares, a synthesis of recent observations and theoretical concepts* **101**, Kluwer Academic Publishers, Dordrecht.
- Barnes, G., Longcope, D.W., Leka, K.D.: 2005, *ApJ* **629**, 561.
- Beveridge, C., Longcope, D.W.: 2005, *Solar Phys.* **227**, 193.
- Biernat, H.K., Heyn, M.F., Semenov, V.S.: 1987, *JGR* **92**, 3392.
- Birn, J., Drake, J.F., Shay, M.A., Rogers, B.N., Denton, R.E., Hesse, M., Kuznetsova, M., Ma, Z.W., Bhattacharjee, A., Otto, A., Pritchett, P.L.: 2001, *JGR* **106**, 3715.

- Biskamp, D., Schwarz, E.: 2001, *Phys. Plasmas* **8**(11), 4729.
- Cargill, P.J., Mariska, J.T., Antiochos, S.K.: 1995, *ApJ* **439**, 1034. doi:10.1086/175240.
- Carmichael, H.: 1964, In: Hess, W.N. (ed.) *AAS-NASA Symposium on the Physics of Solar Flares*, NASA, Washington, DC, 451.
- Dennis, B.R., Zarro, D.M.: 1993, *Solar Phys.* **146**, 177. doi:10.1007/BF00662178.
- Drake, J.F., Swisdak, M., Phan, T.D., Cassak, P.A., Shay, M.A., Lepri, S.T., Lin, R.P., Quataert, E., Zurbuchen, T.H.: 2009, *JGR* **114**, 5111.
- Emslie, A.G., Kucharek, H., Dennis, B.R., Gopalswamy, N., Holman, G.D., Share, G.H., Vourlidas, A., Forbes, T.G., Gallagher, P.T., Mason, G.M., Metcalf, T.R., Mewaldt, R.A., Murphy, R.J., Schwartz, R.A., Zurbuchen, T.H.: 2004, *JGR* **109**, 10104. doi:10.1029/2004JA010571.
- Emslie, A.G., Dennis, B.R., Holman, G.D., Hudson, H.S.: 2005, *JGR* **110**, A11103.
- Erkaev, N.V., Semenov, V.S., Jamitsky, F.: 2000, *Phys. Rev. Lett.* **84**, 1455.
- Forbes, T.G., Priest, E.R.: 1983, *Solar Phys.* **84**, 169. doi:10.1007/BF00157455.
- Forbes, T.G., Priest, E.R.: 1984, In: Butler, D., Papadopoulos, K. (eds.) *Solar Terrestrial Physics: Present and Future*, NASA, ???, 35.
- Forbes, T.G., Priest, E.R.: 1995, *ApJ* **446**, 377. doi:10.1086/175797.
- Forbes, T.G., Malherbe, J.M., Priest, E.R.: 1989, *Solar Phys.* **120**, 285. doi:10.1007/BF00159881.
- Garcia, H.A.: 1994, *Solar Phys.* **154**, 275.
- Giovanelli, R.G.: 1947, *MNRAS* **107**, 338.
- Gorbachev, V.S., Somov, B.V.: 1988, *Solar Phys.* **117**, 77.
- Green, R.M.: 1965, In: Lust, R. (ed.) *Stellar and Solar magnetic fields. Proc. IAU Symp. 22*, North-Holland, Amsterdam, 398.
- Guidoni, S.E., Longcope, D.W.: 2010, *ApJ*. submitted.
- Hannah, I.G., Christe, S., Krucker, S., Hurford, G.J., Hudson, H.S., Lin, R.P.: 2008, *ApJ* **677**, 704. doi:10.1086/529012.

- Heyvarts, J., Priest, E.R., Rust, D.M.: 1977, *ApJ* **216**, 123.
- Hirayama, T.: 1974, *Solar Phys.* **34**, 323.
- Hori, K., Yokoyama, T., Kosugi, T., Shibata, K.: 1997, *ApJ* **489**, 426. doi:10.1086/304754.
- Jiang, Y.W., Liu, S., Liu, W., Petrosian, V.: 2006, *ApJ* **638**, 1140. doi:10.1086/498863.
- Kennel, C.F.: 1987, *JGR* **92**, 13427. doi:10.1029/JA092iA12p13427.
- Kopp, R.A., Pneuman, G.W.: 1976, *Solar Phys.* **50**, 85.
- Kulsrud, R.M.: 2001, *Earth, Planets and Space* **53**, 417.
- Lin, R.P., Hudson, H.S.: 1971, *Solar Phys.* **17**, 412. doi:10.1007/BF00150045.
- Lin, Y., Lee, L.C.: 1994, *Space Science Reviews* **65**, 59. doi:10.1007/BF00749762.
- Lin, Y., Lee, L.C.: 1999, *Phys. Plasmas* **6**, 3131. doi:10.1063/1.873553.
- Linton, M.G., Longcope, D.W.: 2006, *ApJ* **642**, 1177.
- Linton, M.G., Devore, C.R., Longcope, D.W.: 2009, *Earth, Planets, and Space* **61**, 573.
- Longcope, D., Beveridge, C.: 2007, *ApJ* **669**, 621.
- Longcope, D.W.: 2001, *Phys. Plasmas* **8**, 5277.
- Longcope, D.W., Klapper, I.: 2002, *ApJ* **579**, 468.
- Longcope, D.W., Magara, T.: 2004, *ApJ* **608**, 1106.
- Longcope, D.W., Silva, A.V.R.: 1998, *Solar Phys.* **179**, 349.
- Longcope, D.W., Barnes, G., Beveridge, C.: 2009, *ApJ* **693**, 97.
- Longcope, D.W., Guidoni, S.E., Linton, M.G.: 2009, *ApJL* **690**, L18. (LGL09).
- Longcope, D., Beveridge, C., Qiu, J., Ravindra, B., Barnes, G., Dasso, S.: 2007, *Solar Phys.* **244**, 45.
- Masuda, S., Kosugi, T., Hara, H., Tsuneta, S., Ogawara, Y.: 1994, *Nature* **371**, 495. doi:10.1038/371495a0.
- McKenzie, D.E.: 2000, *Solar Phys.* **195**, 381.
- McKenzie, D.E., Hudson, H.S.: 1999, *ApJ* **519**, L93.

- McKenzie, D.E., Savage, S.L.: 2009, *ApJ* **697**, 1569. doi:10.1088/0004-637X/697/2/1569.
- Mewe, R., Gronenschild, E.H.B.M., van den Oord, G.H.J.: 1985, *Astron. and Astrophys Supp.* **62**, 197.
- Miller, J.A., Cargill, P.J., Emslie, A.G., Holman, G.D., Dennis, B.R., LaRosa, T.N., Winglee, R.M., Benka, S.G., Tsuneta, S.: 1997, *JGR* **102**, 14631. doi:10.1029/97JA00976.
- Moore, R.L., Labonte, B.J.: 1980, In: Sheridan, K.V., Dulk, G.A. (eds.) *Solar and Interplanetary Dynamics, IAU Symposium* **91**, 207.
- Neupert, W.M.: 1968, *ApJL* **153**, L59. doi:10.1086/180220.
- Nitta, S., Tanuma, S., Shibata, K., Maezawa, K.: 2001, *ApJ* **550**, 1119.
- Parker, E.N.: 1957, *JGR* **62**(4), 509.
- Petrosian, V., Donaghy, T.Q., McTiernan, J.M.: 2002, *ApJ* **569**, 459. doi:10.1086/339240.
- Petschek, H.E.: 1964, In: Hess, W.N. (ed.) *AAS-NASA Symposium on the Physics of Solar Flares*, NASA, Washington, DC, 425.
- Petschek, H.E., Thorne, R.M.: 1967, *ApJ* **147**, 1157. doi:10.1086/149105.
- Poletto, G., Kopp, R.A.: 1986, In: Neidig, D.F. (ed.) *The Lower Atmospheres of Solar Flares*, National Solar Observatory, ???, 453.
- Priest, E.R., Forbes, T.G.: 2000, *Magnetic reconnection. MHD theory and applications*, Cambridge University Press, ???.
- Priest, E.R., Bungey, T.N., Titov, V.S.: 1997, *Geophys. Astrophys. Fluid Dynamics* **84**, 127.
- Qiu, J., Lee, J., Gary, D.E., Wang, H.: 2002, *ApJ* **565**, 1335. doi:10.1086/324706.
- Qiu, J., Hu, Q., Howard, T.A., Yurchyshyn, V.B.: 2007, *ApJ*. In press.
- Reeves, K.K., Warren, H.P.: 2002, *ApJ* **578**, 590. doi:10.1086/342310.
- Rosner, R., Tucker, W.H., Vaiana, G.S.: 1978, *ApJ* **220**, 643.
- Saba, J.L.R., Gaeng, T., Tarbell, T.D.: 2006, *ApJ* **641**, 1197. doi:10.1086/500631.
- Schwartz, R.: 1996, Nasa sti/recon technical report n, 96, 71448.
- Sheeley, N.R. Jr., Warren, H.P., Wang, Y.M.: 2004, *ApJ* **616**, 1224. doi:10.1086/425126.

- Skender, M., Vršnak, B., Martinis, M.: 2003, *Phys. Rev. E* **68**(4), 046405. doi:10.1103/PhysRevE.68.046405.
- Sonnerup, B.U.O.: 1970, *J. Plasma Phys.* **4**, 161.
- Soward, A.M.: 1982, *Journal of Plasma Physics* **28**, 415.
- Soward, A.M., Priest, E.R.: 1982, *Journal of Plasma Physics* **28**, 335.
- Strong, K.T., Benz, A.O., Dennis, B.R., Poland, A.I., Leibacher, J.W., Mewe, R., Schrijver, J., Simnett, G., Smith, J.B. Jr., Sylwester, J.: 1984, *Solar Phys.* **91**, 325. doi:10.1007/BF00146303.
- Sturrock, P.A.: 1968, In: *IAU Symp. 35: Structure and Development of Solar Active Regions*, 471.
- Sweet, P.A.: 1958, In: Lehnert, B. (ed.) *Electromagnetic Phenomena in Cosmical Physics*, Cambridge University Press, Cambridge, U.K., 123.
- Syrovatskii, S.I.: 1971, *Sov. Phys. JETP* **33**(5), 933.
- Tsuneta, S.: 1996, *ApJ* **456**, L63.
- Tsuneta, S., Masuda, S., Kosugi, T., Sato, J.: 1997, *ApJ* **478**, 787. doi:10.1086/303812.
- Vasyliunas, V.M.: 1975, *Rev. Geophys. and Space Phys.* **13**, 303.
- Vršnak, B., Skender, M.: 2005, *Solar Phys.* **226**, 97. doi:10.1007/s11207-005-5701-3.
- Wang, Y., Zhang, J.: 2007, *ApJ* **665**, 1428. doi:10.1086/519765.
- Warren, H.P.: 2006, *ApJ* **637**, 522. doi:10.1086/497904.
- Warren, H.P., Winebarger, A.R., Hamilton, P.S.: 2002, *ApJL* **579**, L41. doi:10.1086/344921.
- Xu, P., Forbes, T.G.: 1992, *Solar Phys.* **139**, 315. doi:10.1007/BF00159157.